A model coupling biomechanics and fluid dynamics for the simulation of controlled flapping flight

Victor Colognesi, Renaud Ronsse, Philippe Chatelain
UCLouvain; Institute of Mechanics, Materials and Civil Engineering
Louvain-la-Neuve, Belgium

December 8, 2020

Abstract

This paper proposes a multiphysics computational framework coupling bio-mechanics and aerodynamics for the simulation of bird flight. It features a bio-mechanical model based on the anatomy of a bird, that models the bones and feathers of the wing. The aerodynamic solver relies on a vortex particle-mesh method and represents the wing through an immersed lifting line, acting like a source of vorticity in the flow.

An application of the numerical tool is presented in the modeling of the flight of a Northern Bald Ibis (*Geronticus Eremita*). The wing kinematics are imposed based on biological observations and controllers are developed to enable stable flight in closed-loop. Their design is based on a linearized model of flapping flight dynamics. The controller solves an under-determination in the control parameters through minimization. The tool and the controllers are used in two simulations: a first where the bird has to trim itself at a given flight speed, and another where it has to accelerate from a trimmed state to another at a higher speed.

The bird wake is accurately represented. It is analyzed and compared to the widespread frozen-wake assumption, highlighting phenomena that the latter can not capture. The method also allows the computation of the aerodynamic forces experienced by the flier, either through the lifting line method or through control-volume analysis. The computed power requirements at several flight speeds exhibit an order of magnitude and dependency on velocity in agreement with the literature.

1 Introduction

Bird flight has always been a source of inspiration for engineers. Recent advance in localisation technologies led to the discovery of impressive avian behaviors, in particular regarding flight efficiency. The bar-tailed godwit has been found to migrate from Alaska to New-Zealand in a 11000-kilometer long journey, neither stopping nor feeding [1, 2]. It has also been discovered that some swifts remain airborne during up to ten months [3]. Despite a recent boost in interest for the analysis of bird flight, thrived on new sensing and motion capture technologies, the details of what makes such performance possible remain elusive.

Several methods have been developed to shed light on the mechanics of bird flight. The first and natural one is observation and measurement of bird bio-mechanics, flapping gaits or aerodynamics. In this context, flight kinematics have been reported for a few species, as well as gait variations as a function of the flight speed [4, 5, 6]. These work enable to understand how birds adapt their kinematics with respect to their flight speed but do not provide a full understanding of why they do so. Other studies provided data about the power necessary for bird flight [7, 8, 9]. These indicate that birds adapt their kinematics and wing shape in order to keep their power consumption at low level across varying speeds [7]. Such data can be extracted from observations of the bird itself, using high speed cameras or strain gauges.

We note that dynamics information can also be recovered from a bird's wake: the air flow behind a bird can be measured (using e.g. PIV), allowing to analyse its wake [10]. From these measurements, it is also possible to estimate the aerodynamic forces acting on the bird, as done in [11, 12, 13, 14]. Such wake measurements are most often limited to a single plane. Hence, they can not capture out-of-plane derivatives of the velocity. For example, in [12, 13, 14], measurement are performed in a plane normal to the wind velocity and the spanwise vorticity cannot be computed. These studies also rely on models to compute the aerodynamic forces from the measurements. These models imply that the wake is frozen downstream from the bird and are usually based on the identification of a limited number of vortex pairs for the computation of lift. Both of these limitations could lead to imprecision or incompleteness of the results. It has also been shown that commonly-used methods to compute the aerodynamic forces from quantities measured in the wake give inconsistent results both through time and compared to each other [15].

All these works provide precious insight on the flight and wake of a bird but a full understanding of bird flight will more likely be based on a synthetic method. Thus the present work is part of a project aimed towards a numerical model capable of simulating bird flight. The advantages of a detailed model of bird flight and its wake are manifold. First, it allows capturing the continuum of gait variations that occur through varying flight speeds, as simpler models are not sufficient to model the kinematics of birds across flight speeds [11]. It is also perfectly reproducible and allows the analysis of the wake without measurement errors. The consistency of methods to compute the aerodynamic forces from data in the wake at various times and locations can then be tested.

There exist a few numerical models of flapping fliers. Notably, Shim and Kim [16, 17] simulated evolved flying creatures and experimented on various resulting wing shapes. This leads to interesting results but the tools used in that work do not enable a high level of precision concerning the aerodynamic forces. Indeed, the aerodynamic model used in [16, 17] only considers the effect of the instantaneous angle of attack on the lift and drag coefficients and the wake is not taken into account. Another model has been developed by Parslew [18, 19], which predicted different gaits with varying flight speed, as reported in [4]. This model uses blade elements theory, where the lift and drag coefficients are also computed as a function of the local instantaneous angle of attack with a correction accounting for the induced velocity. The wake is not modeled and the feathers are rigidly fixed to the wing bones. Valuable contributions can also be found in the field of computer graphics [20, 21]. In [20], a simplified aerodynamic model is coupled to a more developed bio-mechanical model. It features the same rigid segments as a bird wing and the feathers are both flexible and articulated.

Literature does not propose any model of a flapping flier embodying both a faithful reproduction of bird bio-mechanics and an accurate computation of the aerodynamics and wake. In this paper, we report the development of a new methodology for the simulation of flapping flight. The bio-inspired mechanical model is made to resemble the skeleton of birds. The wings are articulated with the same main degrees of freedom as those of real birds and the plumage is modeled by a limited number of feathers representing the movement of all of them, similarly to the model reported in [20]. The wing aerodynamics are modeled using an immersed lifting line method and the wake is accurately modeled with a state-of-the-art vortex particle-mesh method. The combination of these two methods has already proved to produce reference results, see [22]. Crucially, the vortex particle-mesh method is computationnally efficient and able to capture the development of the wake over large distances [23, 24].

The model is applied to the simulation and control of a bio-mimetic flapping flier. In order to model the flight, the wing kinematics of the flier are determined. Simple closed-loop controllers are implemented to stabilize the flight and reach trim state. They are based on a linearized model of flapping flight aerodynamics that is also presented. The controllers are able to get the flier through transients, such as transitioning between different flight speeds.

The first section of this paper describes the numerical model developed to simulate flapping flight. The flier multi-body model and the aerodynamic solver are presented, as well as the coupling between them. The following section provides a description of the bird that the model aims at representing. An application of the tool is presented in the third section with a description of imposed wing kinematics, the development of a linearized model of flapping flight aerodynamics, and the design of a closed-loop controller for the longitudinal stabilization and trim of the flight. In the fourth section, results are presented for the application of this model to two different scenarios.

2 Methods

The main contribution of this paper is a numerical tool for the simulation of articulated flapping flight. This tool consists in the coupling of a multi-body model and a flow solver, as shown in figure 1. The multi-body model, further explained in section 2.1, takes as input the internal and external forces acting on a multi-body system representing the articulated flier. It then computes its dynamics and provides its kinematics as output. The fluid solver, further explained in section 2.2, requires the kinematics of a lifting line as an input, then computes the flow around it and the aerodynamic forces acting on it. A coupling part, further explained in section 2.3 is required for these two first parts to communicate. On the one hand, from the aerodynamic forces, it computes the resulting forces on the bodies composing the multi-body system. On the other hand, it computes the kinematics of a lifting line starting from the kinematics of the flier's bodies.

Throughout this paper, the frame used follows the usual conventions in aerodynamics: the X-axis is aligned with the free-stream velocity and points in the forward direction of flight, the Y-axis points towards the right wing and the Z-axis points down vertically.

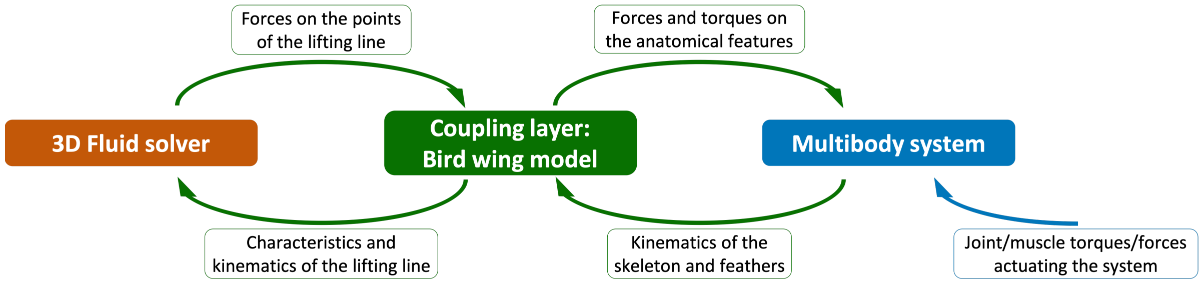

Figure 1: Coupling scheme used between the two solvers

2.1 Articulated flapping flier multi-body model

The multi-body model is handled by an integrator named Robotran [25](www.robotran.be). This software uses symbolic generation to establish the equations of motion of a multi-body system. It also provides an integrator to solve these equations over time. The equations are formulated for a tree-like structure and based on the use of relative joint coordinates. That is, a frame is attached to each body and the joint angles of the degree of freedom of the next body in the tree-like structure is defined in the local frame. Consequently, all the angles presented in the following sections are defined in a local frame. Robotran is able to handle both direct and inverse dynamics but only the former is used in the present application.

The flier model consists of a main body, and two wings. The body is linked to the inertial frame through three translations and three rotations, so that it can be left free in the six degrees of freedom or be blocked in whichever degree of freedom. A wing structure is shown in figure 2. The representation of the wing is inspired from the work of Wu and Popović [20]. It consists of three rigid bodies corresponding to the arm, the forearm and the hand.

The bodies are articulated like follows: the first rigid segment, i.e. the arm, is articulated to the body with three rotations at the shoulder, consequently along the Y, X and Z axes, respectively noted $q_{s,Y}(t)$, $q_{s,X}(t)$ and $q_{s,Z}(t)$. The forearm segment is then articulated to the arm segment at the elbow with a single rotation along the Z axis noted $q_{e,Z}(t)$. The hand segment is articulated to the forearm segment at the wrist through two rotations along the Y and Z axes, noted $q_{w,Y}(t)$ and $q_{w,Z}(t)$. All the rotations occur in single points except the Y rotation of the wrist ($q_{w,Y}$). This rotation (pronation/supination of the forearm) is uniformly spread over the forearm and leads to twist in the wing.

Following an interpolation ansatz, a reduced set of control-feathers represents the plumage and models its deformations. The control-feathers are attached to the bones directly. This representation of feathers is simpler than the one used in [20]. In the present work and in [20], the feathers have the same degrees of freedom (i.e. Z and Y rotations, for spreading and cambering, respectively). However, while the feathers remain straight in this work, they have bending compliance in [20]. The rationale behind this simplification is that we lack an accurate model or data for the feather bending. Still, compliance is captured to a lesser extent by the Y rotation at the root of the feather, which involves a rotational spring in the present work and was locked in [20]. Only the third primary feather (the outermost feather) is rigidly attached to the hand segment.

To ensure a smooth spreading of the feathers as the wing folds and expands, the feathers are coupled to each other with spring-like components, effectively connecting each control-feather to its two neighbors. This emulates the function of the tendons spanning across the roots of adjacent feathers both for body covert feathers [26, 27] and for the remiges (flight feathers) [28]. The elastic nature of the tendon led to a representation by a spring component. Other interactions between bird feathers ensure that they form a continuous surface and do not cross [29]. For the sake of simplicity, the springs representing the tendons are placed at the tip of the feathers, rather than close to

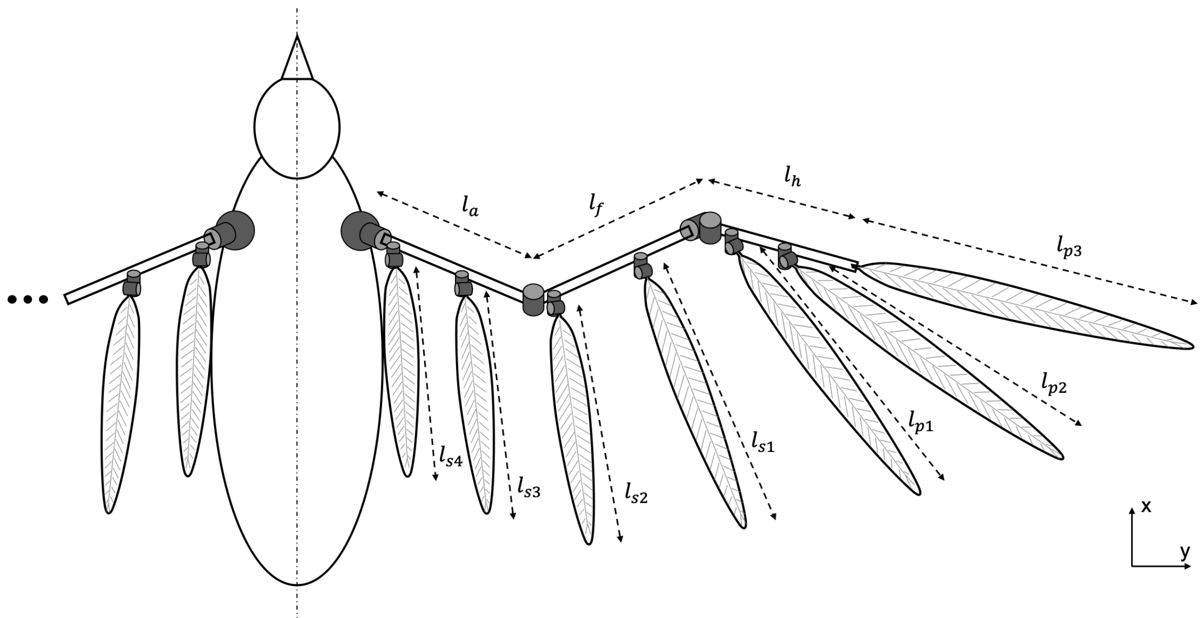

Figure 2: Top view of the multi-body model of the flier's wing. The lengths l_a, l_f and l_h represent respectively the lengths of the arm, forearm and hand segments. The lengths l_{p3}, l_{p2}, l_{p1}, l_{s1}, l_{s2}, l_{s3} and l_{s4} represent the lengths of the three primary and four secondary feathers, respectively.

the root, as seen in actual birds [26, 27, 28]. This provides a realistic model of these interactions and guarantees that the feathers do not cross.

Additionally, the insertion points of the feathers on the bones also behave like rotational springs, essentially generating reaction forces on the plumage when it is experiencing aerodynamic forces. The tip feathers, however, are attached rigidly and remain aligned with their respective hand segment, as it was reported for rock pigeons in [28]. More detail on the forces and moments produced by the springs is given in appendix A.

The mass of the flier is entirely located in the body and the wing bones. The wings are set to constitute 10% of the total mass. This mass is distributed among the bones and they are considered as cylinders of mass for the computation of their inertia matrix. The inertia matrix of the body is computed as the one of an ellipsoid. The feathers are assumed to be massless.

2.2 Flow solver

This work relies on a vortex particle-mesh method combined with lifting lines to solve the aerodynamics and the wake of the bird. This method is based on the vorticity-velocity $\boldsymbol{\omega} - \mathbf{u}$ formulation of the Navier-Stokes equations for incompressible flows. The vorticity is the curl of the velocity $\boldsymbol{\omega} = \nabla \times \mathbf{u}$. An incompressible flow translates to a divergence-free velocity field $\nabla \cdot \mathbf{u} = \mathbf{0}$ and the Navier-Stokes equations can be formulated as:

$$\frac{D\boldsymbol{\omega}}{Dt} = (\nabla \mathbf{u}) \cdot \boldsymbol{\omega} + \nu \nabla^2 \boldsymbol{\omega} \tag{1}$$

where $\dfrac{D}{Dt} = \left(\dfrac{\partial}{\partial t} + \mathbf{u} \cdot \nabla\right)$ is the Lagrangian derivative operator and ν is the kinematic viscosity.

The vorticity field is discretized using particles characterized by a position $\mathbf{x}_p$ and a strength $\boldsymbol{\alpha}_p = \int_{V_p} \boldsymbol{\omega} d\mathbf{x}$, V_p being the material volume assigned to the particle. The convection of the particles and the evolution of their strength are governed by the following equations :

$$\frac{d\mathbf{x}_p}{dt} = \mathbf{u}(\mathbf{x}_p) \tag{2}$$

$$\frac{d\boldsymbol{\alpha}_p}{dt} = \int_{V_p} ((\nabla \mathbf{u}) \cdot \boldsymbol{\omega} + \nu \nabla^2 \boldsymbol{\omega}) d\mathbf{x} \ , \tag{3}$$

which are solved using a third order Runge-Kutta scheme. The velocity field, required to solve the above equations, is recovered by solving the following Poisson equation :

$$\nabla^2 \mathbf{u} = -\nabla \times \boldsymbol{\omega} \ . \tag{4}$$

The vortex particle-mesh method uses a hybrid discretization: the spatial derivatives in the right-hand side of equation 3 are computed on a grid, using fourth order centered finite differences. The grid is also used to solve the Poisson equation 4, using a solver operating in the Fourier space. This allows to use unbounded directions simultaneously with inlet-outlet boundaries [30].

High order schemes are used to pass the information back and forth between the particles and the grid at each time step. The mesh is also used to reset the particles on grid points every few time steps. This operation prevents the clustering or depletion of particles in some areas of the flow. Additionally, this particle discretization does not guarantee the solenoidal property of the vorticity (as it is the curl of velocity). A reprojection operation is thus performed every few timesteps to ensure this condition (20 in the presented simulations). Both operations are further explained in [24]. This method is implemented for massively parallel architectures, using the PPM library [31].

In this method, the flier is represented as a source of vorticity, through an Immersed Lifting Line (ILL) method [32]. This is possible using the assumption that the wings are slender and that the flow around the airfoil is essentially two-dimensional. In this method, the instantaneous lift and drag coefficients C_L and C_D are obtained from the local flow conditions, i.e. local instantaneous angle of attack and Reynolds number, using data from an aerodynamic polar. This application uses an AS6092 airfoil [33]. It is a bird-like airfoil and its polar is available in [33], where it has been computed using XFOIL [34]. This ILL method sheds the vortical structures related to the production of lift. Note that the airfoil drag (i.e. viscous and pressure drag) is captured through the look-up of the drag coefficient C_D and the local flow condition but its vortical signature is not shed in the wake. It has a marginal effect on the local flow along the line but rather only affects the vortex smearing further in the wake, see [32] for more details. The bound circulation $\mathbf{\Gamma}$ is related to the lift vector $\mathbf{L}$ using the Kutta-Joukowski theorem :

$$\mathbf{L} = \rho \mathbf{V} \times \mathbf{\Gamma}$$

where ρ is the air density and $\mathbf{V}$ the local relative velocity vector of the flow with respect to the airfoil. The wing is then represented by a lifting line with bound vortex particles accounting for the circulation. The lifting line also sheds new vortex particles, according to the variations of the circulation, which merge with the existing particles in the flow.

The Kutta–Joukowski theorem is classically derived for a steady two-dimensional potential flow. By using this relationship, we assume that the flow around the airfoil is steady and unseparated. Therefore, the presented method is limited to flight regimes where the unsteady and stall effects can be neglected. While it has not been done in the present study, the evaluation of the lift coefficient can also be performed with lifting line using dynamic stall models, as in [35].

In the present application, the lifting line has the particularity of deforming during the simulation. Even more than deforming, its length will also vary. This implies that the discretization of the lifting lines varies over time. While this is not part of the usual ILL methods, it can be shown that the same method can still be applied with arbitrary time-varying discretization and that the resulting forces and the wake are not affected. Mathematical proof of this statement is presented in appendix B.

An additional force accounting for the body drag is applied at the center of gravity of the body. This force is aligned with the instantaneous velocity of the body and its magnitude is computed as:

$$D_{body} = C_{D,body} \cdot \frac{1}{2} \rho U^2 S_b \tag{5}$$

where $C_{D,body}$ is the drag coefficient of the body, ρ the air density, U the instantaneous relative air velocity with respect to the body and S_b the frontal surface of the body. The values of the frontal surface and the drag coefficient are evaluated following the method proposed by Pennycuick in [36].

2.3 Coupling

The coupling between the multi-body model and the flow solver plays two roles (see figure 1). The first is to provide the multi-body model with the resultant of the aerodynamic forces on each feather. The second is to provide the flow solver with the kinematics of the lifting line, which have to be computed from the position and velocities of the bodies in the multi-body model. This second function captures the morphing of the wing.

The methodology used to pass the forces from the points of the lifting line to the feathers is represented in figure 3. It is a substantial simplification of a continuous distribution of forces and torques on a wing to a set of discrete forces acting on specific bodies (i.e. the feathers represented in the bio-mechanical model). For each point of the lifting line, the closest feather is found. This decomposes the line in a set of sections each corresponding to a single feather. The force acting on the center of each feather is then computed by summing the contributions of the points in its corresponding section as:

$$\mathbf{F}_f = \sum \mathbf{dF}_l$$

where $\mathbf{F}_f$ is the total force acting on a feather and $\mathbf{dF}_l$ is the contribution of a single point of the lifting line. Since the application points of the forces are displaced, an additional torque $\mathbf{M}_f$ is added to the feather. It is computed as:

$$\mathbf{M}_f = \sum \mathbf{dM}_f = \sum \mathbf{\Delta x}_l \times \mathbf{dF}_l$$

where $\mathbf{\Delta x}_l$ is the vector connecting the center of the feather to the point of the lifting line.

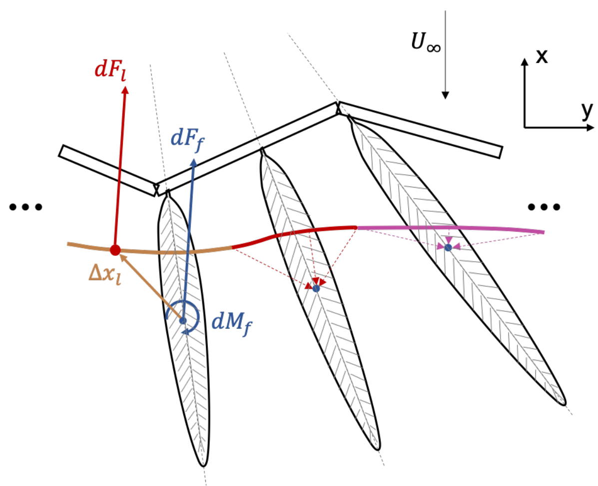

Figure 3: Free-body diagram capturing the equivalence between a force acting at the level of the lifting line to a force an moment acting at the level of one feather.

The instantaneous shape of the lifting line is computed from the positions of the bones and control-feathers composing the multi-body model. This process starts by drawing the contour of the wing. The leading edge first follows the propatagial tendon in a straight line between the shoulder and the wrist. This tendon is part of a muscle spanning from the torso to the hand of the bird. It forms a triangle of skin with the wing bones that is part of the lifting surface. It then goes along the "hand" segment and the outermost feather to the tip of the wing. The trailing edge links the tip of each control-feather from the innermost to the outermost and meets the leading edge at the tip of the wing. The leading and trailing edge are continuous lines that together form the wing surface, from which the lifting line is extracted.

The ILL method requires the lifting line to (i) pass through the quarter of the chord of the wing and (ii) be orthogonal to that chord at each of its points. Condition (i) is generally part of the formulation of the lifting line methods, where the line is the locus of the aerodynamic center of the wing [37, 38]. Furthermore, in aerodynamic polars, the aerodynamic moment is typically defined about the quarter of the chord, since the aerodynamic forces produce a constant moment about this point in the case of a symmetric airfoil. Condition (ii) is mandatory to avoid miscalculations of the surface of the wing.

A first guess for the quarter-chord line can be obtained from a sampling of the leading and trailing edges with a same number of points: it is taken as the line linking the points at the quarter of the distance between corresponding points of the leading and trailing edges. This first guess is however not orthogonal to the chord. Therefore, it is iteratively updated to enforce the orthogonality condition (ii). This iterative process is described in appendix C.

3 Embodiment: the Northern Bald Ibis

While the model presented in this document can be adapted to represent any flapping flier, its main application in this paper will be to model bird flight, and in particular the flight of the Northern Bald Ibis (*Geronticus eremita*). This particular bird has been chosen for its high aspect ratio wing. This improves the validity of the representation of the wing with lifting lines (see section 2.2). It also relies on a non-stop flapping flight mode which is modeled in this work. Finally, this bird is known to migrate in formations where its wake is exploited by followers [39] and the analysis of this phenomenon is one of the motivations for the development of this model. The bones and feather lengths used in the multi-body model are summarized in appendix A. The total mass of the bird is set to 1.2 kg. The body mass is 1.1 kg and 0.05 kg is distributed in the bones of each wing. An example of wing kinematics that the model can output for the ibis is pictured in figure 4.

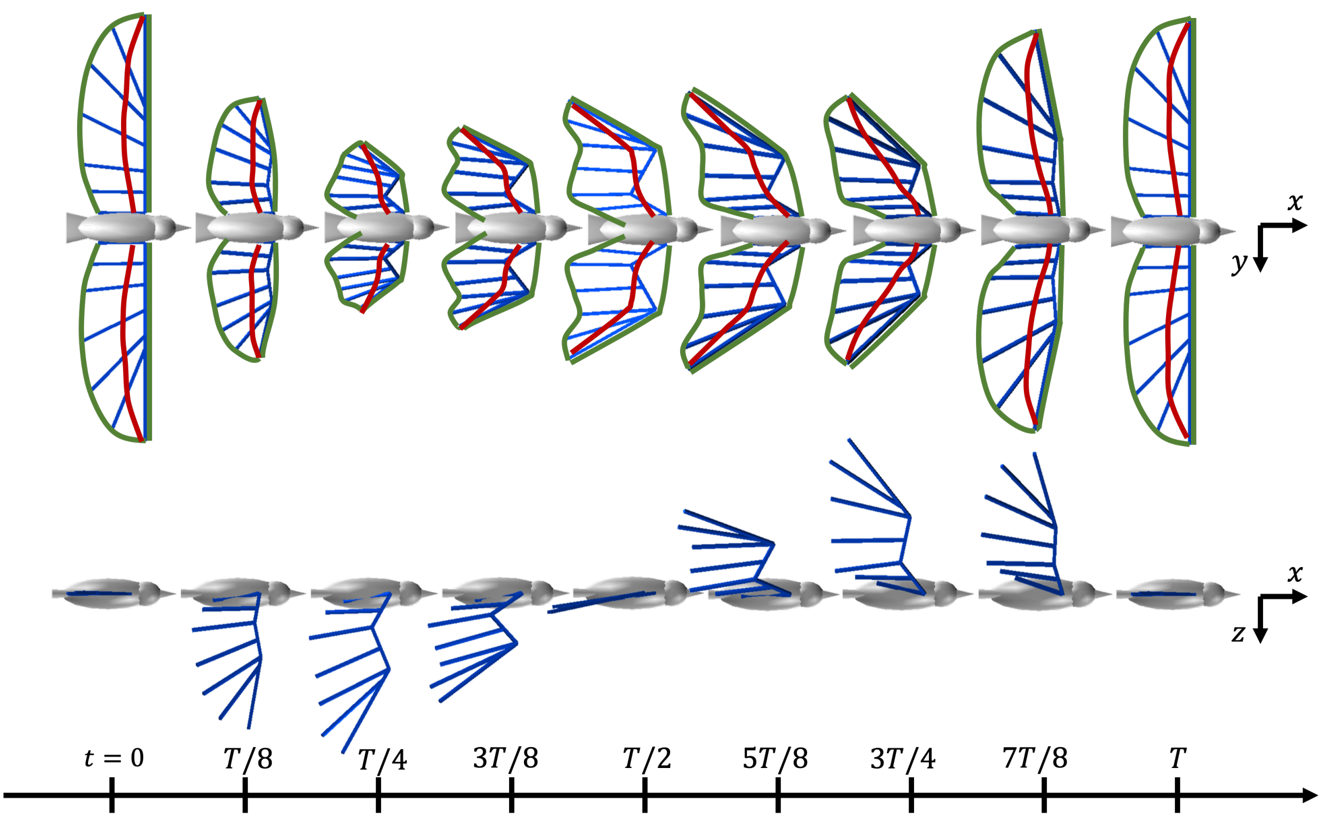

Figure 4: Snapshots of a representative wing kinematics over a flapping cycle. The three rigid segments and the seven control-feathers are represented in blue. The green lines represent the leading and trailing edges. Note that the feathers do not start at the leading edge near the root of the wing. In this region, the leading edge is situated at the level of the propatagial tendon and the feathers are still attached to the wing bones. The red line represents the lifting line along which the wing's aerodynamics are computed.

In order to simulate the flight of the flier, the flapping frequency and the flight velocity need to be determined. For the frequency, a value of 4 wingbeats per second (4 Hz) is chosen. It is approximately the flapping frequency observed for the *Geronticus Eremita* and is a close value to the flapping frequency of birds similar to it [40, 41]. A flight speed of $15\,\mathrm{m\,s^{-1}}$ is selected as a target, i.e. a typical value for this particular bird [39].

The body drag is evaluated for this particular bird following the method presented in [36]. Considering a mass of 1.2 kg – the average mass of the *Geronticus Eremita* – a Reynolds number $Re = 1.37\ 10^5$ and a frontal surface

$S_b = 9.19\ 10^{-3}\ \mathrm{m}^2$ are obtained. From the Reynolds, [36] gives a value for the drag coefficient $C_{D,body} = 0.291$. For a target velocity $U = 15\,\mathrm{m\,s^{-1}}$, following equation 5, the body drag is estimated to $D = 0.369$ N.

4 Closed-loop control of a bio-mimetic flapping flier

In this section, the model described in section 2 is used for the control of longitudinal flapping flight. First, in section 4.1, imposed kinematics are defined for the actuation of the multi-body model. Section 4.2 identifies an open-loop model for the flight dynamics. A linearization of the flight dynamics is performed around an equilibrium identified by minimizing the energy consumption of the bird. Then, in section 4.3 a closed-loop controller is designed based on the identified linear model.

4.1 Wing kinematics

This section is dedicated to the description of the wing kinematics. In particular, the kinematics for the right wing will be described. The ones of the left wing are chosen to be symmetric. Since the kinematics of the skeleton are imposed, the joint torques are ignored in the computations of the motions of the multi-body model. The kinematics are imposed in order to create a flapping motion similar to that of a real bird wing. All the notations for the names of the joint rotations are described in section 2.1.

A first constraint comes from mechanisms in bird wings that couple the rotation of the wrist joint to the one of the elbow joint, effectively maintaining a constant angle between the humerus (i.e. the first rigid segment of the wing) and the carpometacarpus (i.e. the hand segment) [42]. Both bones constituting the forearm (ulna and radius) remain parallel and form a parallelogram with the arm (humerus) and hand (carpometacarpus) bones. This results in a maintained parallelism between the latter two bones, and in the biologically-imposed constraint $q_{w,Z}(t) = -q_{e,Z}(t)$ at any time t, as represented in figure 5. This reduces to five the amount of joint angles that follow an independent kinematic trajectory.

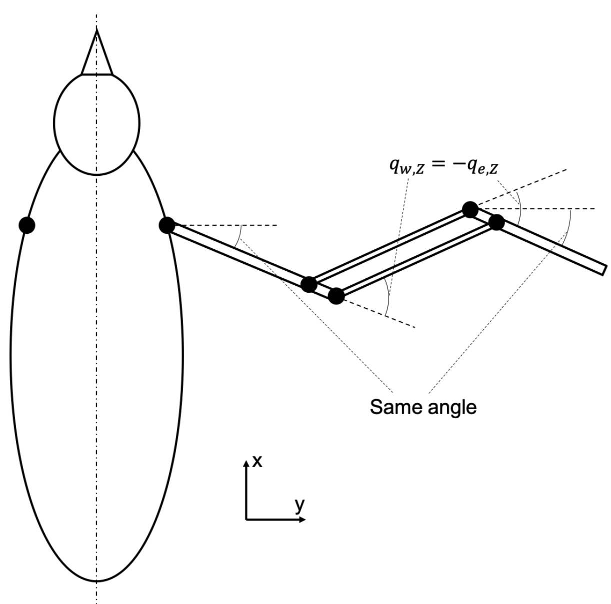

Figure 5: Simplified representation of the mechanical constraint on the wrist rotation

To reduce the dimensionality of the parameter space, each joint angle i is considered to follow an harmonic trajectory $q_i(t)$, with its own amplitude A_i, mean value $q_{0,i}$ and phase $\phi_{0,i}$:

$$q_i(t) = q_{0,i} + A_i \cdot \sin(\omega t + \phi_{0,i}) \tag{6}$$

with $\omega = 2\pi f$ and f being the flapping frequency, identical for each joint. For the five remaining unconstrained joint rotations of the model shown in figure 2, this makes a total of 15 gait parameters to be defined for characterizing a particular kinematic pattern. Table 1 summarizes the explanation for the determination of each kinematic parameter. Throughout this section, each paragraph will explain how some of the parameters are fixed. The word "parallelism" in table 1 refers to the kinematic relationship described in the previous paragraph.

	Shoulder X	Shoulder Y	Shoulder Z	Elbow Z	Wrist Y	Wrist Z
Mean (q_0)	adjusted	independent	independent	adjusted	adjusted	parallelism
Amplitude (A)	independent	independent	adjusted	extension	adjusted	parallelism
Phase (ϕ_0)	reference	follow flow	extension	extension	follow flow	parallelism

Table 1: Summary of the determination of each kinematic parameter.

Since the phases $\phi_{0,i}$ are relative to each other, one of them can be arbitrarily placed, without any consequence on the resulting gaits. Here, we took $\phi_{0,s,X} = 0$ so that $t = 0$ corresponds to the middle of the downstroke. This choice is referred to as "reference" in table 1.

It has been reported that a bird wing will be at its largest span halfway through the downstroke and at its shortest in the middle of the upstroke [4]. This impacts the Z rotation of the shoulder and elbow joints. Since the midpoint of the downstroke corresponds to $\omega t = 2k\pi$, with k being any integer, it implies that the sine function in equation 6 is at an extremum at $\omega t = 2k\pi$, i.e. $\phi_{0,i,Z} = \pm\pi/2$ where the subscript i refers to the shoulder or elbow joint. Since the shoulder folds when $q_{s,Z}(t) > 0$ and the elbow when $q_{e,Z}(t) < 0$, and since $q_{w,Z} = -q_{e,Z}$, one obtains $\phi_{0,s,Z} = -\pi/2$, $\phi_{0,e,Z} = \pi/2$ and $\phi_{0,w,Z} = -\pi/2$.

The maximum span will be reached when the wing is fully extended and the joint angles of the elbow and wrist along the Z axis equal zero. This means that $q_{i,Z}(t = 0) = 0$ for these joints, which implies $A_{e,Z} = -q_{0,e,Z} = A_{w,Z} = q_{0,w,Z}$. The parameters determined using this reasoning are reported as "extension" in table 1.

Another assumption is that the phases of the shoulder and wrist Y rotations are such that the wing will follow the flow. This translates for both of these joints to $\phi_{0,i,Y} = -\pi/2$, since a negative value is desired during the downstroke and a positive one during the upstroke. For the shoulder joint, it means that the wing pitches up during the upstroke and down during the downstroke, thereby reducing the amplitude of the variations of the angle of attack through the flapping period. Regarding the wrist joint, it means that the wing twists during the flapping motion in order to reduce the variations of angle of attack along the span. This assumption is referred to as "follow flow" in table 1.

The remaining parameters are obtained by fitting the wingtip and wrist trajectories to the ones observed in wind tunnel for the pigeon at $14\,\mathrm{m\,s^{-1}}$ in [4]. For the model to be comparable with the reference, a secondary embodiment is performed, using bones and feather lengths representative of a pigeon, i.e. $l_a = 4.54$ cm, $l_f = 5.49$ cm, $l_h = 3.36$ cm and $l_{p,3} = 20$ cm. The values of the remaining parameters are adjusted so that the trajectories roughly agree with the ones of [4].

Figure 6 compares the obtained trajectories of the wingtip and wrist to the reference ones. The difference in the trajectories of the side view of figure 6 comes from some inconsistency in [4]: in the top view, the wingtip passes at the level of the shoulder during the downstroke, while it stays further behind in the side view. Since the wing has a larger span when the tip is at the shoulder level, it appears more optimal to follow the trajectory shown in the top view. This results in the side view in a broader trajectory than the ones described in [4].

Based on the fitted trajectories of figure 6, relationships have been established between the remaining gait parameters. Four of these parameters are kept independent to allow the control of the flier. The main one is the amplitude of the flapping motion $A_{s,X}$ and three others are the mean value and amplitude of the pitching motion and the mean value of the sweeping motion of the shoulder joint: $q_{0,s,Y}$, $A_{s,Y}$ and $q_{0,s,Z}$. Taking the previously stated constraints and these biologically-based observations into account, the following relationships are established for the remaining parameters:

$$\begin{aligned}
q_{0,s,X} &= 0 & q_{0,w,Y} &= 0 \\
A_{s,Z} &= 0.5\,A_{s,X} & A_{w,Y} &= 0.083\,A_{s,X} \\
q_{0,e,Z} &= -0.75\,A_{s,X} & q_{0,w,Z} &= 0.75\,A_{s,X} \\
A_{e,Z} &= 0.75\,A_{s,X} & A_{w,Z} &= 0.75\,A_{s,X}
\end{aligned}$$

These relationships will be used in the rest of this paper. The parameters determined by these equations are referred to as "adjusted" in table 1. The independent parameters are referred to as "independent". We acknowledge that these relations are partly arbitrary, since they are based on the trajectories of two points of the wing for kinematics of a single species at a single flight speed. As a consequence, they likely only hold over a limited range of flight regimes. We do not claim that they accurately represent the very actual kinematics of a bird, but we still consider that they produce realistic gaits.

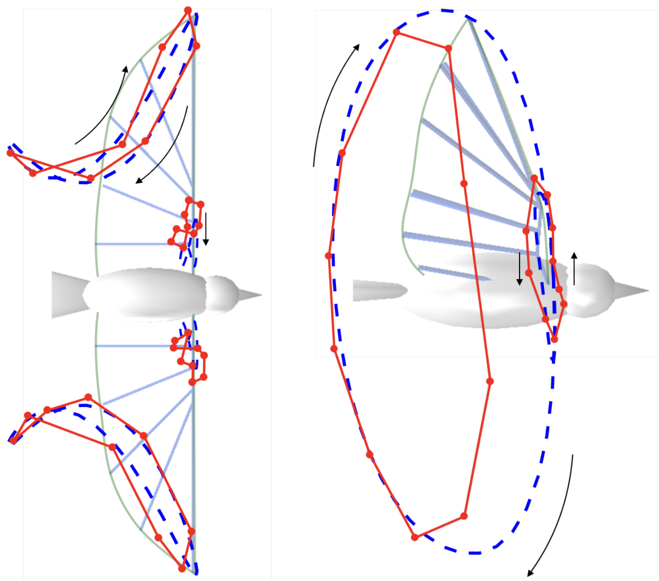

Figure 6: Comparison of the wingtip and wrist trajectories over a flapping cycle obtained from [4] (solid red) and the constrained kinematics obtained in this section (dashed blue). These trajectories are obtained using the following values of the independent gait parameters: $q_{0,s,Y} = 5°$, $A_{s,Y} = 2°$, $A_{s,X} = 60°$ and $q_{0,s,Z} = 30°$. The body represented has roughly the dimensions of a pigeon but is only shown for illustrative purposes.

4.2 Identification of an open-loop model of flapping flight

In section 4.1, we identified four parameters that remained independent to specify the wing kinematics. These parameters can be used as outputs of controllers in order to stabilize the flight of a bio-mimetic flier. In order to understand how the values of these parameters can be computed, one needs to identify an open-loop model of flapping flight. This model relates the longitudinal flight dynamics to the values of these four independent parameters. In longitudinal flight, three degrees of freedom have to be considered: the vertical position (along Z), the horizontal, streamwise position (along X) and the pitch angle (rotation around Y).

Since flapping flight is intrinsically periodic and oscillatory, so must be the velocities and pitch angle. However, in order to simplify the open-loop model, this oscillatory behavior will be ignored. This is achieved by averaging the measured quantities over the last flapping period. That is, in place of any measured variable $f(t)$, its mean value over the last flapping period $\bar{f}(t)$ is considered and computed at any time t as:

$$\bar{f}(t) = \int_{t-T}^{t} f(t')dt' \tag{7}$$

where T is the flapping period. The variable f can represent a force, a torque, a velocity or an angle. The open-loop model thus relates the period-averaged values of the forces and velocities of the flier to the independent gait parameters, while ignoring the oscillations around the average.

For linear control to be applicable, the flight dynamics need to be linearized around an equilibrium. This equilibrium regime has been chosen as the one that minimizes power consumption. To find it, several values of one of the four gait parameters are tested, and for each of these values, the other three are adapted so as to get a force equilibrium. The power consumption is computed at each of these equilibrium points by multiplying the joint torque of each actuated joint (i.e. the elbow, the shoulder and the joint) by its angular velocity, and averaging the power over a flapping cycle according to equation 7. During a flapping cycle, there are short periods of time where the instantaneous power is negative. These contributions to the energy consumption are also included. While this may differ from other bio-locomotion works where the positive part of the instantaneous power is used (see e.g. [19, 43]), it is reported in [44] that the main wing muscles store and release up to 9 % of their net mechanical work. In our case, it is equivalent to considering that energy can be stored as elastic energy and released without any losses. The search for minimum power is represented in figure 7. The equilibrium point is chosen with a value of 5 degrees for the parameter $A_{s,Y}$ and the corresponding values for the remaining three.

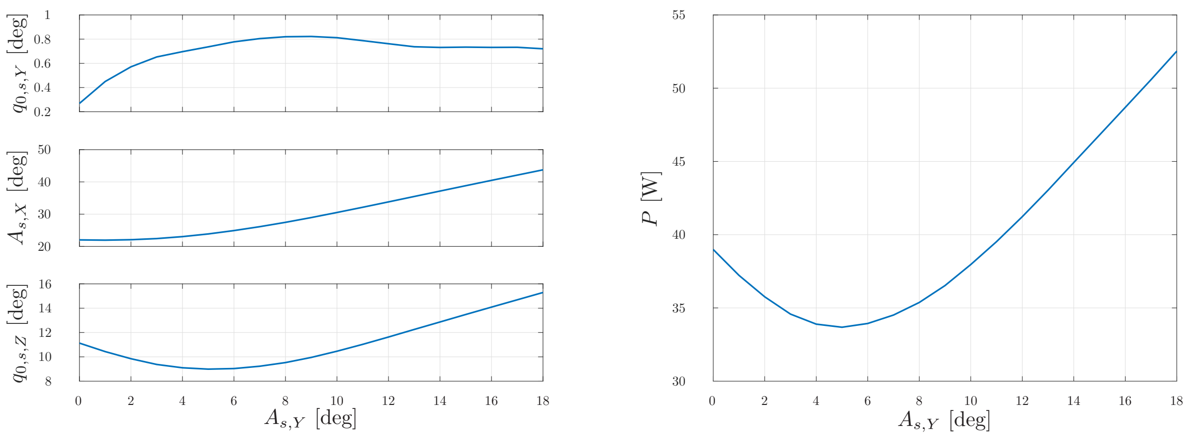

(a) Gait parameters

(b) Power

Figure 7: Power consumption of the flier at various equilibrium states. In panel (a) are represented the values of the equilibrium gait parameters for a varying value of $A_{s,Y}$. For each value of $A_{s,Y}$, the corresponding values of $q_{0,s,Y}$, $A_{s,X}$ and $q_{0,s,Z}$ leading to the equilibrium are represented. The period-averaged power is presented in panel (b).

The open-loop model for longitudinal flight around the chosen equilibrium point relates the values of the independent kinematic parameters to the average forces and moment in the longitudinal plane through a 3×4 sensitivity matrix noted $\boldsymbol{S}$. That is, if the forces and moment are represented by a vector $\bar{\mathbf{F}} = \left[\bar{F}_Z, \bar{F}_X, \bar{M}_Y\right]^T$ and the gait parameters by a vector $\mathbf{q} = [q_{0,s,Y}, A_{s,Y}, A_{s,X}, q_{0,s,Z}]^T$, we have that:

$$\bar{\mathbf{F}} = \boldsymbol{S} \cdot \mathbf{q} \, . \tag{8}$$

The outputs of the model are the vertical and horizontal velocities v_Z and v_X and the pitch angle θ of the flier. To obtain these, it is assumed that there is a separation of timescales between the rate of change of the period-averaged forces and the flapping period. In this case, the averaging of equation 7 can be neglected and the following equations can be written:

$$\left\{ \begin{array}{rcl} \dot{\bar{v}}_Z & = & \dfrac{\bar{F}_Z}{m} \\ \dot{\bar{v}}_X & = & \dfrac{\bar{F}_X}{m} \\ \ddot{\bar{\theta}} & = & \dfrac{\bar{M}_Y}{I_Y} \end{array} \right. \tag{9}$$

where m and I_Y are respectively the mass of the flier and its moment of inertia along the Y axis.

Additionally, the contribution to the forces of the mean pitch angle $\bar{\theta}$ is considered. This angle is the only degree of freedom to have a significant impact on the dynamics. Since the body force does not depend on its inclination in this model, and the pitching rotation of the body causes an equal rotation of the shoulder, the influence of $\bar{\theta}$ is equivalent to that of $q_{0,s,Y}$ (i.e. the mean value of the pitching rotation of the shoulder joint). As a result, equation 8 is modified into:

$$\bar{\mathbf{F}} = \boldsymbol{S} \cdot \left(\mathbf{q} + \begin{pmatrix} \bar{\theta} \\ 0 \\ 0 \\ 0 \end{pmatrix} \right) \tag{10}$$

where the relative rotation of the wing with respect to the body ($q_{0,s,Y}$) is replaced by its absolute rotation with respect to a fixed frame ($q_{0,s,Y} + \bar{\theta}$).

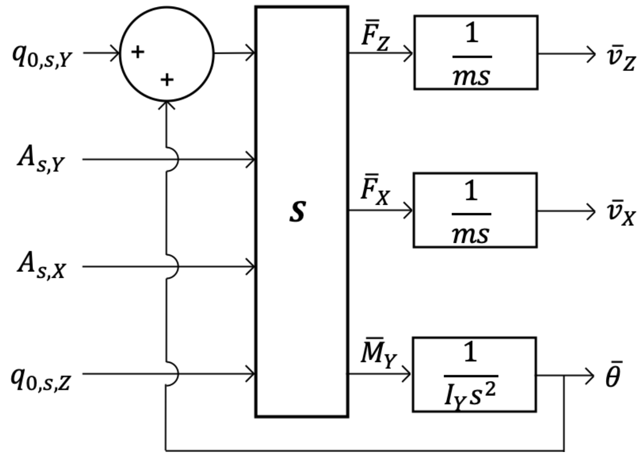

Figure 8: Open-loop model used to capture the flapping flight dynamics. To the left, the independent gait parameters are taken as inputs, and to the right, the outputs are the horizontal and vertical velocities and the pitch angle.

Figure 8 represents equations 9 and 10 in a block diagram. In order to complete the identification of the open-loop model, the sensitivity $\boldsymbol{S}$ of the system to the gait parameters has to be quantified. For this, simulations are carried out with discrete values of the gait parameters around the equilibrium. In each of these simulations, the flier's body is maintained fixed and horizontal. Vertical and horizontal forces and pitching moment are measured and averaged over the fourth flapping period as in equation 7. At that point, the average force has reached its final value, after the wake has finished developing. The average forces and moment are related to the varying gait parameters and linear regressions are extracted from the data to complete the linear model. The matrix $\boldsymbol{S}$ then contains the slopes of these linear regressions. Figure 9 illustrates this method by representing the forces and moment as a function of the four gait parameters in the case of the northern bald ibis (see section 3), although the same method would remain valid for any flier.

4.3 Closed-loop stabilization of longitudinal flight

Closed-loop controllers are designed to compute the values of the independent gait parameters leading to longitudinal stabilization the flight. A separate controller is assigned to each degree of freedom of the flight so that their gains can be computed independently. Each of these controllers outputs the force or moment that the flier has to produce in the corresponding degree of freedom. The value of the gait parameters leading to the desired force needs to be computed. This is equivalent to solving the system $\boldsymbol{S} \cdot \mathbf{q} = \bar{\mathbf{F}}$, with $\bar{\mathbf{F}}$ being the (period-averaged) forces vector prescribed by the controllers.

Since $\boldsymbol{S}$ is a 3×4 matrix, multiple solutions exist to this system. One of them is given by using the pseudo-inverse $\boldsymbol{S}^+$ of $\boldsymbol{S}$ [45]. In the present case, since $\boldsymbol{S}$ is a full rank matrix, we obtain $\boldsymbol{S}^+ = \boldsymbol{S}^T \left(\boldsymbol{S}\boldsymbol{S}^T\right)^{-1}$, and $\boldsymbol{S} \cdot \boldsymbol{S}^+ = \boldsymbol{I}$. A property of the pseudo-inverse matrix is that it ensures the norm of the solution to be minimal. That is, for a given target force $\bar{\mathbf{F}}$ from the controllers, we have that $\boldsymbol{S} \cdot \mathbf{q} = \boldsymbol{S} \cdot \boldsymbol{S}^+ \bar{\mathbf{F}} = \bar{\mathbf{F}}$ and that $|\mathbf{q}| = \sqrt{q_{0,s,Y}^2 + A_{s,Y}^2 + A_{s,X}^2 + q_{0,s,Z}^2}$ is minimum. This means that the controller will use the smallest possible departures from the equilibrium parameters. Since the equilibrium is chosen at a minimum of power consumption, it makes sense that the controller outputs values of the gait parameters that are the closest possible to the ones at the equilibrium.

Additionally, the value obtained for $q_{0,s,Y}$ is modified to cancel the contribution of the pitch angle shown in equation 10. This is simply done by subtracting the value $\bar{\theta}$, giving that to obtain a target force $\bar{\mathbf{F}}$, the gait parameters $\mathbf{q}$ are computed as:

$$\mathbf{q} = \boldsymbol{S}^+ \cdot \bar{\mathbf{F}} - \begin{pmatrix} \bar{\theta} \\ 0 \\ 0 \\ 0 \end{pmatrix} \tag{11}$$

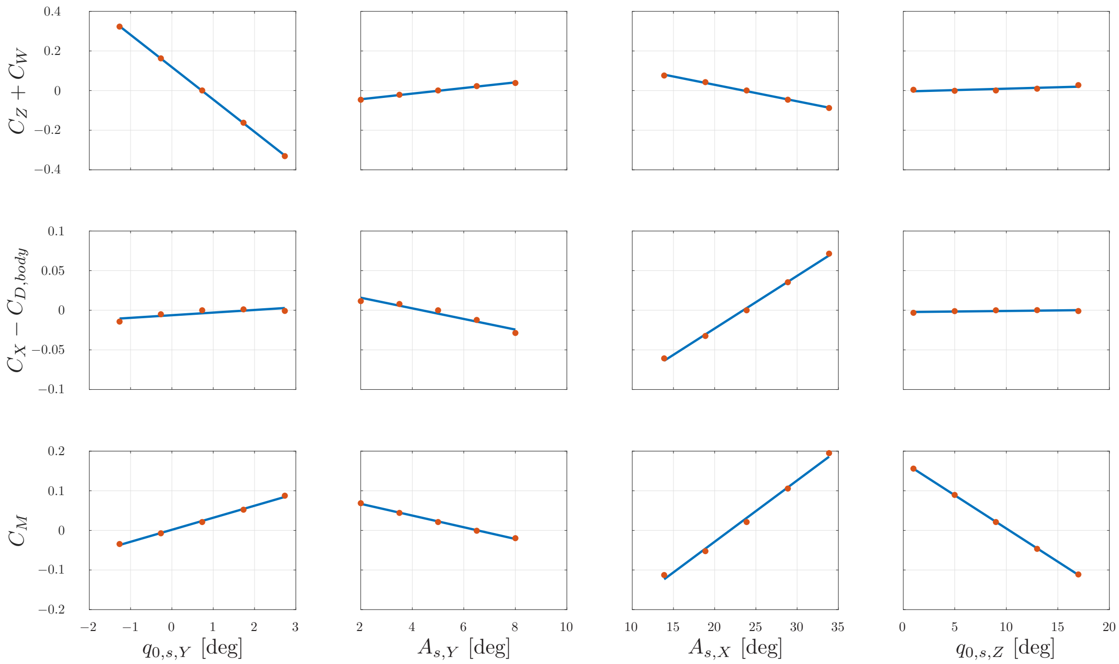

Figure 9: Influence of the independent gait parameters on the longitudinal dynamics. The red dots represent the discrete values extracted from the simulations and the blue line represents linear regressions of these data. The forces are adimentionalized using $\frac{1}{2}\rho U^2 S$ and the moment using $\frac{1}{2}\rho U^2 S\bar{c}$ where ρ is the density of air, U is the flight velocity ($15\,\mathrm{m\,s^{-1}}$), S and $\bar{c}$ are the wing surface and mean aerodynamic chord mid-downstroke. C_W is the adimentionalization of the weight, and $C_{D,body}$ is the body drag coefficient.

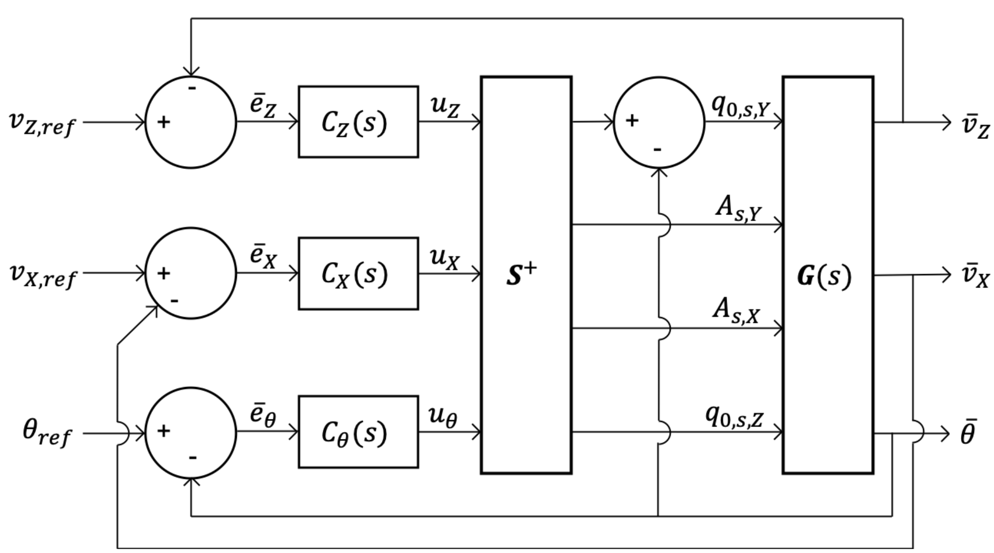

Figure 10: Closed-loop control scheme used to stabilize the flier in all three degrees of freedom. The block $\boldsymbol{G}(s)$ represents the open-loop model that is detailed in figure 8.

The resulting global control scheme is represented in figure 10. The controllers take as input their corresponding error, i.e. e_Z, e_X or e_θ obtained by subtracting the period-averaged values of the velocities and pitch angle to the reference values. They output the reference forces to be achieved using variations of the gait parameters. These variations are computed by a multiplication with the pseudo-inverse $\boldsymbol{S}^+$ of the sensitivity matrix. The pitch angle is finally subtracted following equation 11 to cancel its contribution to the dynamics.

Putting together the open-loop model of figure 8 and the closed-loop scheme of figure 10, and knowing that $\boldsymbol{S} \cdot \boldsymbol{S}^{+} = \boldsymbol{I}$, the following transfer functions can be written:

$$\bar{v}_{Z/X}(s) = \frac{C_{Z/X}(s)\frac{1}{m}}{s + C_{Z/X}(s)\frac{1}{m}} \; v_{Z/X,ref}(s), \tag{12}$$

$$\bar{\theta}(s) = \frac{C_{\theta}(s)\frac{1}{I_Y}}{s^2 + C_{\theta}(s)\frac{1}{I_Y}} \; \theta_{ref}(s) \tag{13}$$

For the two translation degrees of freedom (with transfer function shown in equation 12), a PI controller is used as closed-loop controller, i.e.

$$C_{Z/X}(s) = \frac{k_I}{s} + k_P$$

An integral term is mandatory here to compensate the errors due to the linearization of the model and the proportional term allows a faster response. The denominator of the transfer function is then:

$$Den_{Z/X}(s) = s^2 + s\; k_P \frac{1}{m} + k_I \frac{1}{m} \tag{14}$$

Critical damping is synthesized as a closed-loop behavior. Therefore, the denominator should have the form:

$$Den(s) = s^2 + 2as + a^2 \tag{15}$$

where a is the double pole of the transfer function and has yet to be determined. Putting together equations 14 and 15, the closed-loop gains are obtained as:

$$k_P = 2am$$

and

$$k_I = a^2 m$$

For the pitch controller to have a single closed-loop pole like both other controllers, together with no steady-state error, it requires the use of a PID controller rather than a PI. Indeed, only an integral term can ensure a zero steady-state error and since the denominator of the transfer function of equation 13 has a second order term, it becomes a third degree polynomial such that a controller with three gains is required to place the three poles in closed-loop, i.e.

$$C_{\theta}(s) = s\; k_D + k_P + \frac{k_I}{s}$$

The denominator of the closed-loop transfer function from equation 13 is then:

$$Den_{\theta}(s) = s^3 + s^2\; k_D \frac{1}{I_Y} + s\; k_P \frac{1}{I_Y} + k_I \frac{1}{I_Y} \tag{16}$$

To impose critical damping, the coefficients are obtained by identifying equations 16 to the expression $(s+a)^3 = s^3 + 3as^2 + 3a^2 s + a^3$, i.e.

$$k_D = 3aI_Y \;,$$

$$k_P = 3a^2 I_Y \text{ and}$$

$$k_I = a^3 I_Y \;.$$

The value of the pole a of the transfer functions has yet to be chosen. For the hypotheses underlying the open-loop model to remain valid, there needs to be a separation of time scales between the response time of the transfer functions ($\sim \frac{1}{a}$) and the flapping period T. Furthermore, since the feedback only uses the mean value of the state variables over the last flapping period, the control schemes are only valid if the time scales are properly separated. To satisfy this condition, a value of $a = \frac{1}{5T} = 0.8\,\mathrm{s}^{-1}$ is chosen for both translations. For the pitch, however, a higher value of $a = \frac{1}{3T} = 1.3\,\mathrm{s}^{-1}$ is chosen in order to increase the authority of the controller. The rationale behind this synthesis is that the pitching motion is unstable in open-loop, and the flier experiences difficulties to stabilize with less pitching authority.

5 Results

In this section, the articulated flapping flier model and its controller will be tested in two different situations. In section 5.1, the flier is flying in a trimmed state and its aerodynamics and wake can be analyzed. In section 5.2, the flier is tasked to follow a step of reference velocity and accelerate from a velocity below the design point of the controller to one above that point. The power consumption of the flier in both of these scenarios is computed and compared with values from the literature in section 5.3.

In both simulations, the computational domain encompasses the flier and its wake. It moves at a constant horizontal velocity of $15\,\mathrm{m\,s^{-1}}$. It is thus an inertial frame with a flow imposed through it at $U_{inflow} = -15\,\mathrm{m\,s^{-1}}$ in the X direction in both scenarios. The fluid properties are that of air at sea level, i.e. the density is $\rho = 1.225\,\mathrm{kg\,m^{-3}}$, and the kinematic viscosity is $\nu = 1.48\ 10^{-5}\,\mathrm{m^2\,s^{-1}}$. Considering the mean aerodynamic chord of the bird's wing at the middle of the downstroke[1], $\bar{c} \simeq 0.18\,\mathrm{m}$, the chord Reynolds number is $Re = \frac{U\bar{c}}{\nu} \simeq 1.8\ 10^5$. In both scenarios, the bird uses a controller designed to operate around a forward velocity of $15\,\mathrm{m\,s^{-1}}$.

5.1 Stable trimmed flight

In a first simulation, the flier is tasked with finding an equilibrium, i.e. trimming its flight regime, based on averaged diagnostics as explained earlier. At the start of the simulation, the CG of the flier is artificially maintained in a fixed position for four flapping periods, in order to allow the wake to be settled. During this time, it uses kinematics that produce a zero average force on a period. This initial gait is found using another dedicated controller tasked with finding the required kinematic parameters. After the flier is set loose, the forces are expected to change because it oscillates and this impacts the dynamics. Thus the flier undergoes a transient. During this transient, the controllers modify the kinematics in order to ensure that the average velocities tend to zero (which is not equivalent to the average force being equal to zero). After the transient, the flier reaches trimmed flight.

The vortex method provides a representation of the wake of the flier in trimmed state. It is represented in figures 11 and 12. In figure 11, the wake shows well-defined wing tip vortices as well as root vortices. The latter have been observed in both bird [12, 13, 14, 46] and bat [14] flight. They are due to a decrease or increase of the lift distribution in the body or in the tail. Since the vorticity only forms closed contours, any spanwise variation of circulation results in the shedding of vorticity in the wake. In reality, the body and the tail of a bird form a streamlined body that produces lift and has a circulation. In the present simulations, in the absence of body, the circulation is forced to drop to zero at the root of the wings. Hence stronger vortices are shed than if the circulation could keep a non-zero value at the wing-body junction. Recent work [46] even observed that the body-tail ensemble has a circulation larger than the one at the root of the wing for a gliding bird, resulting in vortices of opposite sign to the ones shed in our simulations. The root vortices present in the simulations are thus stronger than they should and do not accurately represent the physics of a real flapping flier.

Figure 12 compares the wake of the flier obtained in the simulation with the one that would be predicted using frozen-wake assumption. The "frozen" wake is obtained by taking snapshots of the near wake (i.e. the wake in the region close to the flier) at various instants and concatenating them. This produces a wake in a frozen state, that does not evolve through time. This representation, while not quantitative, allows a qualitative evaluation of the frozen-wake assumption. The overall shape of the wake remains the same in both cases but 3D effects corresponding to the time variation of the wing circulation occur in the actual wake and are not visible in the frozen one. Such an effect is depicted in figure 13. In the regions of the wake that correspond to periods of lower lift, the tip vortices tend to rise because of vertical velocity induced by the spanwise vorticity. The root vortices have a very different behavior in the actual wake than in the frozen one. Since they constitute a pair of strong vortices at a close distance, they induce high velocities on each other, which causes them to raise in the simulation, while they remain at the same altitude in the frozen wake. However, as their intensity is larger than it should, this specific behavior of the root vortices should not be used to invalidate the frozen wake assumption. One should rather examine the differences in the tip vortices.

Figure 14 shows the total aerodynamic forces and moment during a flapping period. As expected, these forces are periodic. The averaged dynamics show that the flier is at equilibrium. That is, the vertical force F_Z averages to minus the weight of the flier (since it is defined as pointing downwards) and both the horizontal force F_X and

[1] Since this value changes constantly during the flapping motion as the wing deforms, the choice of taking it at the middle of the downstroke is arbitrary but it is still representative.

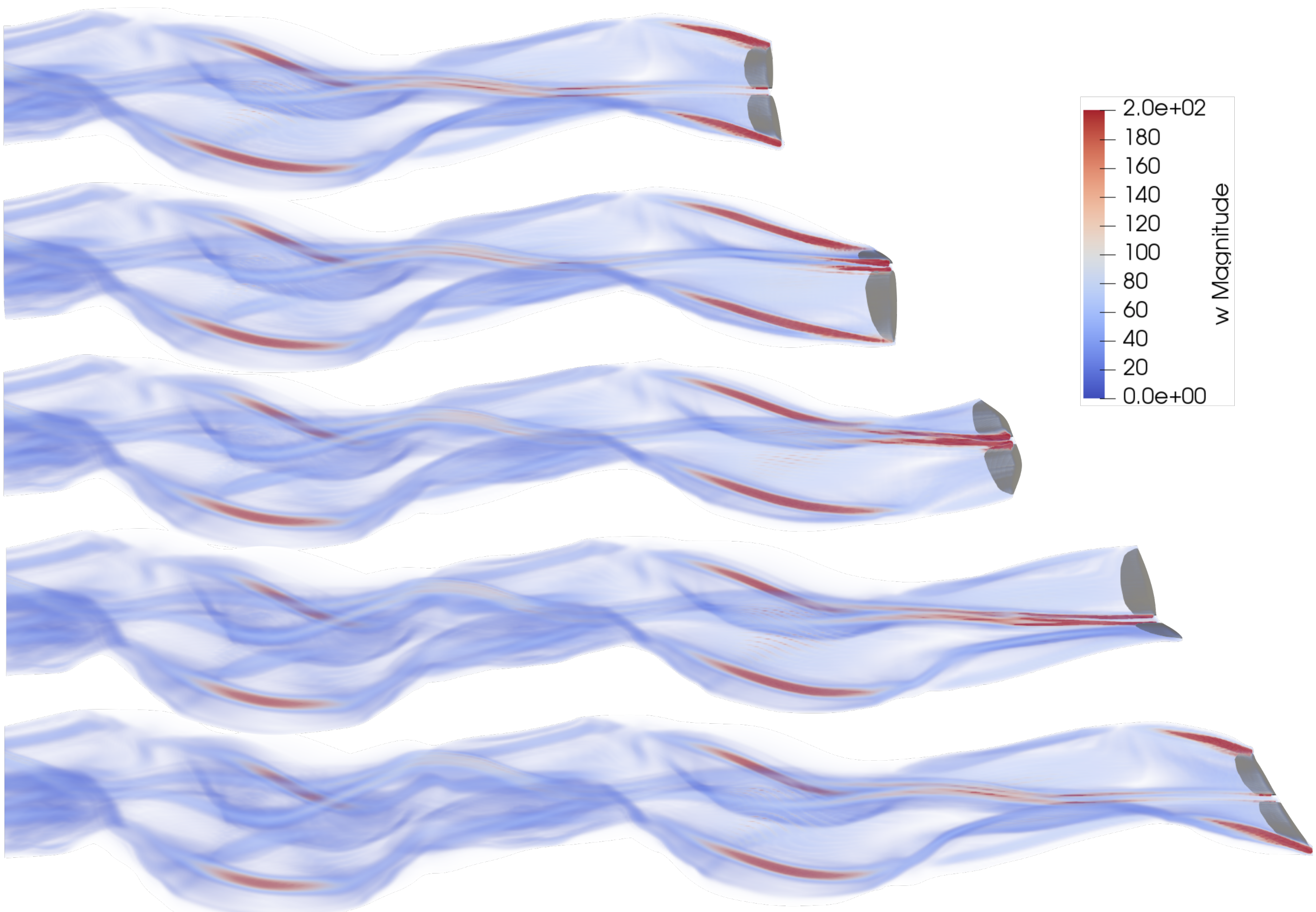

Figure 11: Volume rendering of the vorticity magnitude in the wake of a flapping flier at various instants of its flight. From top to bottom, the snapshots correspond to $t/T = 0, 0.25, 0.5, 0.75$ and 1.

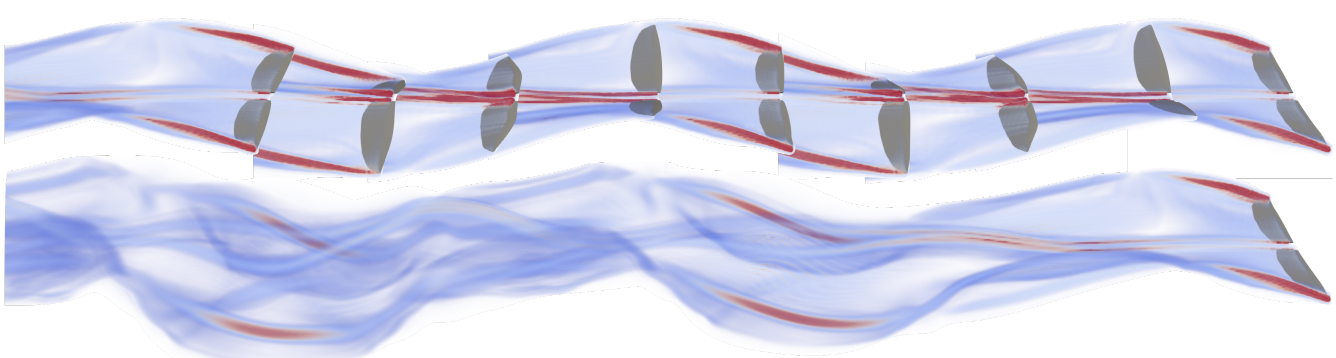

Figure 12: Comparison of the vorticity magnitude in the wake of the flapping flier (lower panel) versus what the frozen-wake assumption would predict (upper panel).

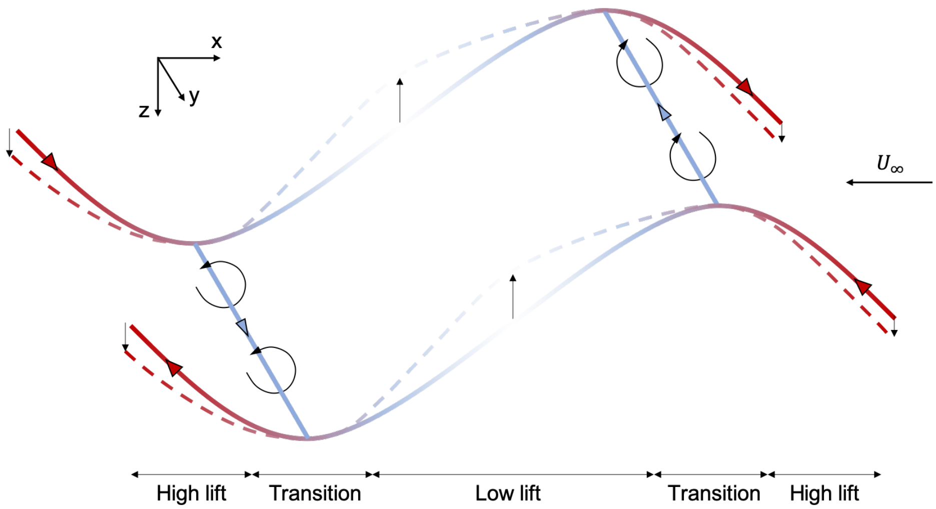

Figure 13: Effect of spanwise vorticity on the tip vortices produced in periods of lower lift. The full lines represent the position of the wingtip vortices that the frozen-wake assumption would predict. The dashed lines represent the deformation of these vortices under the influence of velocities induced by the spanwise vorticity shed during transitions between high and low lift fractions of the flapping period.

the pitching moment M average to zero. Lift is always positive, reaches a maximum around the middle of the downstroke ($t/T \simeq 0$) and gets close to zero during the upstroke ($0.25 < t/T < 0.75$). Net thrust is exclusively produced in the downstroke ($t/T < 0.25$ and $t/T > 0.75$).

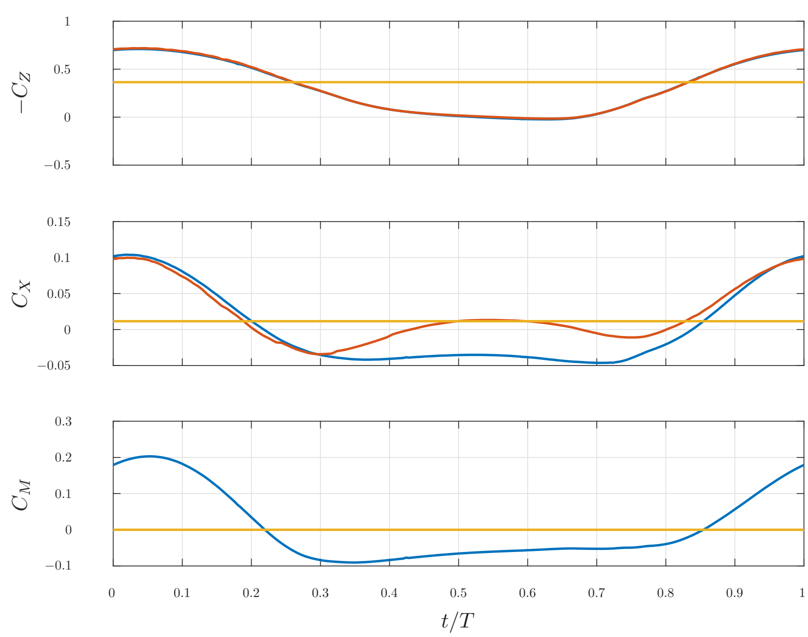

Figure 14: Total aerodynamic forces and moment over a flapping period. In blue are the forces from the lifting line method, in red are the forces recomputed from the wake structures and in yellow are the target forces (weight for the vertical force, body drag for the horizontal force, zero for the pitching moment). $C_Z = F_Z/(q \cdot S)$ is the vertical force coefficient. $C_X = F_X/(q \cdot S)$ is the horizontal force coefficient. $C_M = M/(q \cdot S \cdot \bar{c})$ is the pitching moment coefficient. The dynamic pressure $q = \frac{1}{2}\rho V^2$, the wing surface S and the mean aerodynamic chord mid-downstroke $\bar{c}$ are used for the adimensionalisation.

Figure 14 compares two techniques to compute the unsteady forces produced by the flier. A first one relies on the integral of aerodynamic forces along the ILL, and a second one uses a control volume approach. The latter uses conservation of momentum in a control volume around a flying object, and vector analysis to provide a formulation easily applicable for vortex methods. This formula is reported in [47] and provided in appendix D for the sake of completeness. The match between the results of both techniques is an indicator that all the exchanges of momentum between the wing and the flow have been accurately computed. The difference between the curves for the horizontal force (C_X) is due to the absence of aerodynamic signature for the drag in our simulations. This leads to a higher value for the thrust in the forces measured in the wake, especially during the upstroke where the airfoil drag is at its highest. The vortex signature of drag has recently been added in the flow solver [32] and will be included in future work. The fact that the model allows to accurately capture the momentum in the wake of the flier means that the simulation tool can be used to test experimental methods used to measure the aerodynamic forces acting on a flying bird.

The kinematics are also periodic and the flier follows an oscillating motion. Since the amplitude of the oscillations is relatively small with respect to its velocity, the trajectory appears leveled for a stationary observer. But if the average velocity of the center of gravity is substracted, the resulting trajectory exhibits a loop as in figure 15a. Still, the amplitude of the oscillations is small compared to the size of the flier (the mean aerodynamic chord at mid-downstroke is about 0.18 m). The pitch angle oscillations are also small as it can be seen in figure 15b.

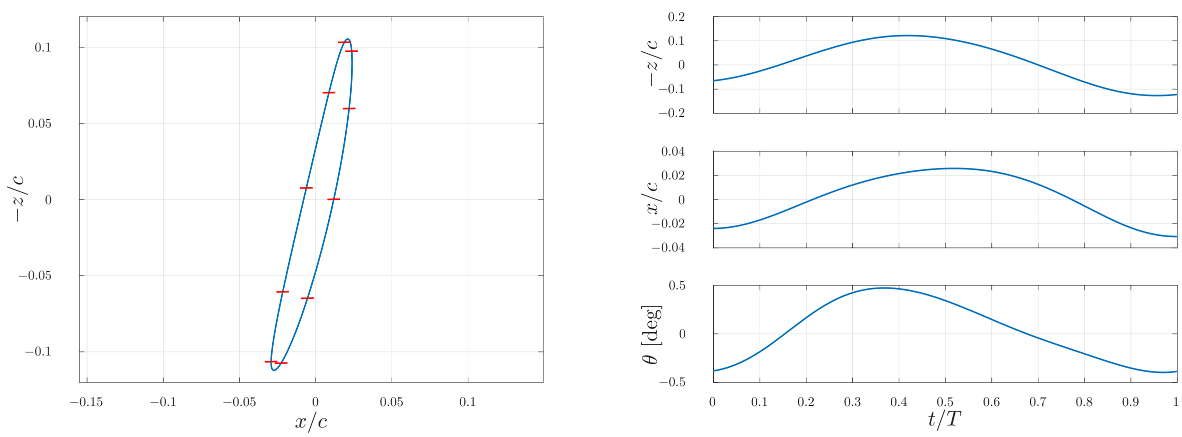

(a) Trajectory (b) Position

Figure 15: Trajectory over one flapping period (a), and position and pitch angle (b). The red lines in the trajectory represent the pitch angle of the bird. The X axis pointing towards the front of the bird, the figure represents a trajectory for a flier going from left to right.

5.2 Step of target flight speed

This section presents a simulation where the flier is tasked with changing its flight speed. In this simulation, it first flies at a velocity of $-1\,\mathrm{m\,s^{-1}}$ in the domain in the X direction. Since a flow is imposed through the computational domain at a velocity of $-15\,\mathrm{m\,s^{-1}}$ as in section 5.1, this is equivalent to flying at $14\,\mathrm{m\,s^{-1}}$. For 20 seconds, it is tasked to remain stable at a velocity of $-1\,\mathrm{m\,s^{-1}}$ in the domain. After 20 seconds, the reference velocity goes from $-1\,\mathrm{m\,s^{-1}}$ to $1\,\mathrm{m\,s^{-1}}$ over 2 seconds, which is equivalent to flying at $16\,\mathrm{m\,s^{-1}}$. After this transition, the flier is tasked to remain stable at a velocity of $1\,\mathrm{m\,s^{-1}}$.

For the first second of the simulation, the flier is artificially constrained to fly straight at $-1\,\mathrm{m\,s^{-1}}$ to ease the stabilization at that flight speed while the wake develops. It is then set free and quickly settles to a trimmed flight. At 20 seconds, it starts to accelerate. Although the controller has been designed to achieve independent control for all three degrees of freedom, this stands true only if the flier is in stable horizontal flight at the design velocity of $15\,\mathrm{m\,s^{-1}}$. Since the flier is not flying at this design velocity at the time it has to accelerate, coupling between the degrees of freedom are expected. The change of kinematics imposed by the controller in response to the change of reference velocity thus also disturbs the equilibrium in the vertical direction and in rotation. As a result, the flier's vertical velocity turns positive. Its pitch angle also varies. After the transient, the flier settles back to a trimmed flight at $1\,\mathrm{m\,s^{-1}}$.

Figure 16a shows a perturbation of around $1\,\mathrm{m\,s^{-1}}$ for the vertical velocity v_Z. It also shows a large perturbation of around $-30°$ for the pitch angle. The step is clearly visible for the v_X part, where it starts at -1 and ends at +1, as tasked. The value of the vertical velocity v_Z varies with the same time scale as v_X.

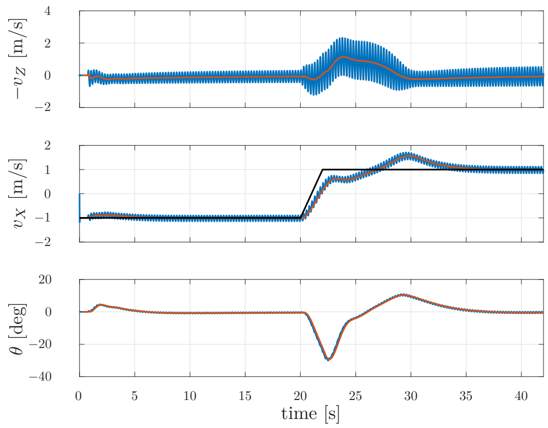

(a) Kinematic variables

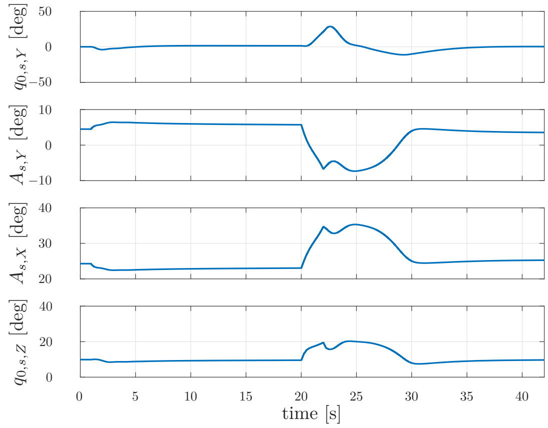

(b) Control parameters

Figure 16: Evolution of the kinematic variables (a) and the control parameters of the controller (b). Panel (a) reports the instantaneous value of the objectives in blue and their mean value over the previous period in red. The reference horizontal velocity is represented in black. Panel (b) pictures the gait control parameters through the whole simulation.

5.3 Comparison of the power consumption with literature data

In this section, the power consumption of the bird in the two flight scenarios is compared to real values reported in the literature. The only experimental result regarding the energy expenditure of the Northern Bald Ibis is found in the work of Bairlein *et al.* [48]. It reports the total energy expenditure of ibises over a whole flight. Instantaneous power consumption can also be extrapolated from data on other birds through allometric relationships. Such equations are found in the work of Norberg [49] and Schmidt-Nielsen [50] (also reported by Butler [51]). Expressions for the minimum power and minimum cost of transport ($COT = P/(W \cdot V)$) can be found in [51]. These same values as well as the velocities at which they are respectively achieved are given in [49]. The allometric relationships are given in table 2.

	P_{min} [W]	V_{Pmin} [$\mathrm{m\,s^{-1}}$]	COT_{min} [–]	V_{COTmin} [$\mathrm{m\,s^{-1}}$]
Norberg [49]	$10.9 \cdot m^{1.19}$	$8.9 \cdot m^{0.21}$	$0.105 \cdot m^{-0.036}$	$11.8 \cdot m^{0.21}$
Butler [51]	$50.7 \cdot m^{0.72}$	–	$0.2053 \cdot m^{-0.3}$	–

Table 2: Allometric relationships for the minimum power P_{min} and cost of transport COT_{min} and their corresponding flight speeds V taken from [49, 51]. The mass is expressed in kg.

In the simulations, the power is computed in the way described in section 4.2, i.e. by summing the product of the joint torque and angular velocity for each driven joint, and averaging the sum over a flapping period. The simulations provide data for three different forward velocities: 14, 15 and $16\,\mathrm{m\,s^{-1}}$. The power is computed for the trimmed flight at each flight speed and compared with the output of the expressions of table 2. The cost of transport is obtained by dividing the power by the corresponding velocity and the weight of the bird. The values are compared in table 3.

From a first look at table 3, we can see that the values for the power and COT are within the range of the values provided by the allometric expressions. The range of values from [48] is higher but represents an average over a

	Norberg [49]	Butler [51]	Bairlein [48]	Present work		
				$14\,\mathrm{m\,s^{-1}}$	$15\,\mathrm{m\,s^{-1}}$	$16\,\mathrm{m\,s^{-1}}$
P [W]	13.54	57.81	82.5 – 224.4	26.66	33.79	38.63
COT [–]	0.1043	0.1944		0.1618	0.1914	0.2051

Table 3: Power and cost of transport as obtained in the simulations, through allometric expressions [49, 51] and from experimental data [48].

whole flight, and includes the costs of take-off and landing. Since the allometric values represent the minimum power and COT, the ones from the simulations should be higher. However, since it was assumed that energy could be stored during the flapping cycle as elastic energy, and that it could be released without any losses, our computation of the power most probably underestimates the actual value. Nevertheless, the agreement, within the same order of magnitude, is remarkable.

From [49], the velocities corresponding to the minimum power and COT are evaluated at 9.30 and $12.26\,\mathrm{m\,s^{-1}}$, respectively. Since the velocities in the simulations are higher than that, it is expected for both the power and the cost of transport to increase with the velocity, which is indeed observed.

6 Conclusions and perspectives

The main contribution of this work is a numerical model for the simulation of flapping flight. This model is built upon a skeletal model of birds, replicating its structure and degrees of freedom. The model is able to produce realistic looking motions and compares favorably with captured gaits of real birds.

The flight aerodynamics are handled by a state-of-the-art vortex particle-mesh code, where the wings are represented by lifting lines. These can compute the aerodynamic forces precisely for slender wings, with much lower computational costs than wing resolved CFD. An original method has been developed to extract a lifting line from leading and trailing edges of a wing. Note that it is not trivial to enforce the defining properties of the lifting line – i.e. that it has to be orthogonal to the chord and pass through the quarter of it at each of its points. If not, it represents a wing different than the one desired. The vortex particle-mesh method allows to accurately represent the wake of the flier over long distances, which is not the case in existing bird models. The aerodynamic forces can also be extracted from the wake, and fit properly with the forces output by the lifting line model, thus validating the exchanges of momentum between the wing and the fluid.

Controllers have been implemented to simulate trimmed flight. The flier is able to reach stable flight in the three longitudinal degrees of freedom, at various flight speeds, and it is able to handle the transient states between two flight speeds. Notably, stabilization of the flapping flight was achieved without the use of a tail, since we assigned that task to wing kinematics and control strategies. While it certainly has an impact on the stability and the maneuvering capability of the bird, this indicates that the tail is not strictly required for stable flapping flight, as reported in [12].

Flight can be analyzed once trim state is reached. The vortex wake features the same structures as the ones reported through measurements on birds in wind tunnel, i.e. essentially tip and root vortices, see e.g. [12, 13, 14, 46]. The tip vortices show differences in behavior compared to the frozen-wake assumption. Regarding the root vortices, the absence of a body causes an abrupt decrease of circulation at the root of the wing, resulting in strong vortices that induce strong velocities on each other.

To sum-up the implications of using a tail- and body-less model, one task of the tail – control and stabilize the flight – can be performed by closed-loop controllers. But the body-tail ensemble also forms a streamlined body that has a circulation and produces lift [46]. The absence of this ensemble between the wings creates vortices stronger than the ones observed in reality.

The power consumption of the flier is computed in all three simulated trimmed states. The values for the power consumption and the cost of transport are compared with values reported in the literature. The order of magnitude is respected for both the power consumption and the cost of transport, and they further obey a similar dependency as a function of the flight speed.

This simulation tool opens up new possibilities. On the one hand, modeling the wake of a flapping flier allows to further analyze the wake and maybe improve the measurements that can be done in wind tunnel. It also allows to simulate formation flight – which migratory birds use at a great advantage to achieve long flights with minimal energy expense – using of the kinetic energy of the wake, as reported in [39]. A faithful modelization of birds wake such as the one presented here is mandatory to understand the details of formation flight, since the wake of a flapping flier is strongly 3-dimensional and time-evolving, as it has been shown in section 5.1. The control-volume analysis of the wake allows the accurate computation of the aerodynamic forces acting on the flier. While the results were promising, they can be much improved by adding the signature of the profile drag in the flow. This can be done using a new feature of the flow solver that has been recently developed [32]. We note that this control-volume analysis could be used to improve the precision of the aerodynamic forces computation from experimental measurements.

On the other hand, the faithful skeletal model can be improved to include a muscular or even neuro-muscular model. Such a model, based on birds' anatomy, enables a better quantification of the required power for flapping flight. A campaign of simulations at various flight speeds would then produce power curves, which could in turn be compared with measurements on actual birds [7, 8, 9]. A proper quantification of the required power can also be used as an objective function for an optimization process leading to the identification of theoretically optimal gaits.

Acknowledgments

Victor Colognesi is supported by a FRIA grant from the Fonds de la Recherche Scientifique de Belgique (F.R.S.-FNRS).

This work is part of a project supported by the ARC program of the Federation Wallonie-Bruxelles (grant number 17/22-080, RevealFlight).

Computational resources have been provided by the Consortium des Equipements de Calcul Intensif (CECI), funded by the Fonds de la Recherche Scientifique de Belgique (F.R.S.-FNRS) under Grant No. 2.5020.11 and by the Walloon Region.

The present research also benefited from computational resources made available on the Tier-1 supercomputer of the Federation Wallonie-Bruxelles, infrastructure funded by the Walloon Region under the grant agreement 1117545

References

[1] Anders Hedenström. Extreme endurance migration: what is the limit to non-stop flight? *PLoS biology*, 8(5):e1000362, 2010.

[2] Robert E Gill Jr, T Lee Tibbitts, David C Douglas, Colleen M Handel, Daniel M Mulcahy, Jon C Gottschalck, Nils Warnock, Brian J McCaffery, Philip F Battley, and Theunis Piersma. Extreme endurance flights by landbirds crossing the pacific ocean: ecological corridor rather than barrier? *Proceedings of the Royal Society of London. Series B: Biological Sciences*, 276(1656):447–457, 2008.

[3] Anders Hedenström, Gabriel Norevik, Kajsa Warfvinge, Arne Andersson, Johan Bäckman, and Susanne Åkesson. Annual 10-month aerial life phase in the common swift apus apus. *CURRENT BIOLOGY*, 26(22):3066–3070, 2016.

[4] Bret W. Tobalske and Kenneth P. Dial. Flight kinematics of the black-billed magpies and pigeons over a wide range of speeds. *The Journal of Experimental Biology*, 199(2):263–280, 1996.

[5] Tyson L Hedrick, Bret W Tobalske, and Andrew A Biewener. Estimates of circulation and gait change based on a three-dimensional kinematic analysis of flight in cockatiels (nymphicus hollandicus) and ringed turtle-doves (streptopelia risoria). *Journal of Experimental Biology*, 205(10):1389–1409, 2002.

[6] Bret W Tobalske, Tyson L Hedrick, and Andrew A Biewener. Wing kinematics of avian flight across speeds. *Journal of Avian Biology*, 34(2):177–184, 2003.

[7] Kenneth P. Dial, Andrew A Biewener, Bret W Tobalske, and D.R. Warrick. Mechanical power output of bird flight. *Nature*, 390(6655):67, 1997.

[8] Bret W. Tobalske, T.L. Hedrick, K.P. Dial, and A.A. Biewener. Comparative power curves in bird flight. *Nature*, 421(6921):363, 2003.

[9] Bret W. Tobalske. Biomechanics of bird flight. *Journal of Experimental Biology*, 210(18):3135–3146, 2007.

[10] GR Spedding, Anders Hedenström, and Mikael Rosén. Quantitative studies of the wakes of freely flying birds in a low-turbulence wind tunnel. *Experiments in Fluids*, 34(2):291, 2003.

[11] GR Spedding, Mikael Rosén, and Anders Hedenström. A family of vortex wakes generated by a thrush nightingale in free flight in a wind tunnel over its entire natural range of flight speeds. *Journal of experimental biology*, 206(14):2313–2344, 2003.

[12] L. C. Johansson and A. Hedenström. The vortex wake of blackcaps (*Sylvia atricapilla* l.) measured using high-speed digital particle image velocimetry (dpiv). *Journal of Experimental Biology*, 212(20):3365–3376, 2009.

[13] P. Henningson, F. T. Mujires, and A. Hedenström. Time-resolved vortex wake of a common swift flying over a range of flight speeds. *Journal of The Royal Society Interface*, 8(59):807–816, 2010.

[14] Florian T. Muijres, L. Christoffer Johansson, Melissa S. Bowlin, York Winter, and Anders Hedenström. Comparing aerodynamic efficiency in birds and bats suggests better flight performance in birds. *PloS one*, 7(5):e37335, 2012.

[15] E. Gutierrez, D. B. Quinn, D. D. Chin, and D Lentink. Lift calculations based on accepted wake models for anumal flight are inconsistent and sensitive to vortex dynamics. *Bioinspiration & Biomimetics*, 12(1):016004, 2016.

[16] Yoon Sik Shim, Sun Jeong Kim, and Chang Hun Kim. Evolving flying creatures with path-following behavior. In *ALife IX: Proceedings of the 9th International Conference on the Simulation and Synthesis of Living Systems*, pages 125–132. Citeseer, 2004.

[17] Yoon-Sik Shim and Chang-Hun Kim. Evolving physically simulated flying creatures for efficient cruising. *Artificial life*, 12(4):561–591, 2006.

[18] Ben Parslew and William J. Crowther. Simulating avian wingbeat kinematics. *Journal of Biomechanics*, 43(16):3191–3198, 2010.

[19] Ben Parslew. Predicting power-optimal kinematics of avian wings. *Journal of The Royal Society Interface*, 12(102):201440953, 2015.

[20] Jia-chi Wu and Zoran Popović. Realistic modeling of bird flight animations. *ACM Transactions on Graphics (TOG)*, 22(3):888–895, July 2003.

[21] Eunjung Ju, Jungdam Won, Jehee Lee, Byungkuk Choi, Junyong Noh, and Min Gyu Choi. Data-driven control of flapping flight. *ACM Transactions on Graphics (TOG)*, 32(5):151, 2013.

[22] Philippe Chatelain, Stéphane Backaert, Grégoire Winckelmans, and Stefan Kern. Large eddy simulation of wind turbine wakes. *Flow, Turbulence and Combustion*, 91(3):587–605, 2013.

[23] Philippe Chatelain, Matthieu Duponcheel, Denis-Gabriel Caprace, Yves Marichal, and Grégoire Winckelmans. Vortex particle-mesh simulations of vertical axis wind turbine flows: from the airfoil performance to the very far wake. *Wind Energy Science*, 2(1):317, 2017.

[24] Philippe Chatelain, Alessandro Curioni, Michael Bergdorf, Diego Rossinelli, Wanda Andreoni, and Petros Koumoutsakos. Billion vortex particle Direct Numerical Simulations of aircraft wakes. *Computer Methods in Applied Mechanics and Engineering*, 197(13):1296–1304, Feb 2008.

[25] Nicolas Docquier, Antoine Poncelet, and Paul Fisette. Robotran: a powerful symbolic generator of multibody models. *Mechanical Sciences*, 4(1):199–219, 2013.

[26] J.N. Langley. On the sympathetic system of birds, and on the muscles which move the feathers. *The Journal of physiology*, 30(3-4):221–252, 1903.

[27] Dominique G. Homberger and Kumudini N. de Silva. Functional microanatomy of the feather-bearing integument: Implications for the evolution of birds and avian flight. *American Zoologist*, 40(4):553–574, 2000.

[28] Tobin L. Hieronymus. Flight feather attachment in rock pigeons (columba livia): covert feathers and smooth muscle coordinate a morphing wing. *Journal of Anatomy*, 229(5):631–656, 2016.

[29] Alexander Kovalev, Alexander E. Filippov, and Stanislav N. Gorb. Unzipping bird feathers. *Journal of The Royal Society Interface*, 11(92):20130988, 2014.

[30] Philippe Chatelain and Petros Koumoutsakos. A Fourier-based elliptic solver for vortical flows with periodic and unbounded directions. *Journal of Computational Physics*, 229(7):2425–2431, 4 2010.

[31] I. F. Sbalzarini, J. H. Walther, M. Bergdorf, S. E. Hieber, E. M. Kotsalis, and P. Koumoutsakos. PPM A highly efficient parallel particle mesh library for the simulation of continuum systems. *J. Comput. Phys.*, 215:566–588, jul 2006.

[32] Denis-Gabriel Caprace, Grégoire Winckelmans, and Philippe Chatelain. An immersed lifting and dragging line model for the vortex particle-mesh method. *Theoretical and Computational Fluid Dynamics*, 34:21–48, 2020.

[33] Gavin K. Ananda and Michael S. Selig. Design of bird-like airfoils. In *2018 AIAA Aerospace Sciences Meeting*, page 0310, 2018.

[34] Mark Drela. Xfoil: An analysis and design system for low reynolds number airfoils. In *Low Reynolds number aerodynamics*, pages 1–12. Springer, 1989.

[35] Denis-Gabriel Caprace, Philippe Chatelain, and Grégoire Winckelmans. Wakes of rotorcraft in advancing flight: A large eddy simulation study. *Physics of Fluids*, 32(8):087107, 2020.

[36] C. J. Pennycuick, Holliday H. Obrecht, and Mark R. Fuller. Empirical estimates of body drag of large waterfowl and raptors. *Journal of Experimental Biology*, 135(1):253–264, 1988.

[37] Jackson T. Reid and Douglas F. Hunsaker. A general approach to lifting-line theory, applied to wings with sweep. In *AIAA Scitech 2020 Forum*, 2020.

[38] WF Phillips and DO Snyder. Modern adaptation of Prandtl's classic lifting-line theory. *Journal of Aircraft*, 37(4):662–670, 2000.

[39] Steven J. Portugal, Tatjana Y. Hubel, Johannes Fritz, Stefanie Heese, Daniela Trobe, Bernhard Voelkl, Stephen Hailes, Alan M. Wilson, and James R. Usherwood. Upwash exploitation and downwash avoidance by flap phasing in ibis formation flight. *Nature*, 505(7483):399–402, 01 2014.

[40] C. J. Pennycuick. Predicting wingbeat frequency and wavelentgh of birds. *Journal of Experimental Biology*, 150(1):171–185, 1990.

[41] C. J. Pennycuick. Wingbeat frequency of birds in steady cruising flight: new data and improved predictions. *Journal of Experimental Biology*, 199(7):1613–1618, 1996.

[42] R. J. Vazquez. The automating skeletal and muscular mechanisms of the avian wing (aves). *Zoomorphology*, 114(1):59–71, 1994.

[43] Siddhartha Verma, Guido Novati, and Petros Koumoutsakos. Efficient collective swimming by harnessing vortices through deep reinforcement learning. *Proceedings of the National Academy of Sciences*, 115(23):5849–5854, 2018.

[44] Bret W Tobalske and Andrew A Biewener. Contractile properties of the pigeon supracoracoideus during different modes of flight. *Journal of Experimental Biology*, 211(2):170–179, 2008.

[45] Roger Penrose. A generalized inverse for matrices. *Mathematical proceedings of the Cambridge philosophical society*, 51(3):406–413, 1955.

[46] James R. Usherwood, Jorn A. Cheney, Jialei Song, Shane P. Windsor, Jonathan P. J. Stevenson, Uwe Dierksheide, Alex Nila, and Richard J. Bomphrey. High aerodyamic lift from the tail reduces drag in gliding raptors. *Journal of Experimental Biology*, 223(3), 2020.

[47] F. Noca, D. Shiels, and D. Jeon. A comparison of methods for evaluating time-dependent fluid dynamic forces on bodies, using only velocity fields and their derivatives. *Journal of Fluids and Structures*, 13(5):551–578, Jul 1999.

[48] Franz Bairlein, Johannes Fritz, Alexandra Scope, Ilse Schwendenwein, Gabriela Stanclova, Gertjan van Dijk, Harro AJ Meijer, Simon Verhulst, and John Dittami. Energy expenditure and metabolic changes of free-flying migrating northern bald ibis. *PloS one*, 10(9):e0134433, 2015.

[49] UM Lindhe Norberg. Flight and scaling of flyers in nature. *Flow Phenomena in Nature*, 1:120–154, 2007.

[50] Knut Schmidt-Nielsen. Energy cost of swimming, flying, and running. *Science*, 177(4045):222–228, Jul 1972.

[51] Patrick J. Butler. The physiological basis of bird flight. *Philosophical Transactions of the Royal Society B: Biological Sciences*, 371(1704):20150384, 2016.

A Properties of the Northern Bald Ibis model

The lengths of the bones and feathers used to represent the Northern Bald Ibis are reported in table 4. Subscripts a, f and h refer to the arm, forearm and hand respectively. Subscripts $p\_$ and $s\_$ refer to the primary and secondary feathers. The primary feathers are the ones attached to the hand and are numbered from the wrist to the tip. The secondary feathers are the ones between the body and the wrist and are numbered from the wrist to the root of the wing.

Symbol	l_a	l_f	l_h	l_{p3}	l_{p2}	l_{p1}	l_{s1}	l_{s2}	l_{s3}	l_{s4}
Value [m]	0.134	0.162	0.084	0.25	0.275	0.25	0.225	0.2	0.175	0.15

Table 4: Lengths of the bones and of the feathers for the ibis.

The model uses two types of springs. The feathers are connected with their neighbors through spring-like components. These springs are free to rotate around both their attach points, producing a force aligned with the line passing through these points. The force for the i^{th} link is purely elastic and its norm F_i is computed with the equation:

$$F_i = K_i \cdot (L_i - L_{0,i})$$

where L_i and $L_{0,i}$ are respectively the distance between the attach points and a reference length, and K_i is the stiffness constant of the spring. The orientation of F_i is for each attach point in the direction of the other. The values of $L_{0,i}$ are 0 for each spring, except for the one linking the last secondary feathers of the right and left wings. For this spring, the value is $L_{0,s4-s4} = 0.05$ m. The value of K_i for each spring are given in table 5. The subscripts of the values correspond to the feathers linked by the spring. The subscript $s4 - s4$ corresponds to the spring connecting the last secondary feather of the right and left wings.

Symbol	K_{p3-p2}	K_{p2-p1}	K_{p1-s1}	K_{s1-s2}	K_{s2-s3}	K_{s3-s4}	K_{s4-s4}
Value [N/m]	100	100	100	100	200	300	500

Table 5: Stiffness values of the springs connecting the feathers

Each feathers is also connected to the bone through two rotational springs, except the last primary that is fixed. The torque $T_{X,i}$ of the i^{th} joint along the local X axis is governed by the following equation:

$$T_{X,i} = -K_X \cdot (\phi_{X,i} - \phi_{X,0,i}) - C_X \cdot \dot{\phi}_{X,i}$$

where K_X is the stiffness constant, $\phi_{X,i}$ and $\dot{\phi}_{X,i}$ are the joint angle, expressed in radians, and its time derivative, and C_X is a dissipation constant. The values of K_X and C_X are $K_X = 8$ Nm and $C_X = 0.04$ Nms for each joint. Only the attach point of the first secondary feather has a non-zero value for $\phi_{X,0}$. For the rotation $q_{w,Y}$ to be spread over the forearm, the reference rotation of this feather is equal to half of this rotation. Hence, we have that $\phi_{X,0,s1} = q_{w,Y}/2$.

The torque $T_{Y,i}$ of the i^{th} joint along the local Y axis is purely dissipative and is governed by the equation:

$$T_{Y,i} = -C_Y \cdot \dot{\phi}_{Y,i}$$

where C_Y is a dissipation constant and $\dot{\phi}_{Y,i}$ is the joint angular velocity along the Y axis expressed in radians per second. For each joint, the value of C_Y is 0.04 Nms.

B Independence on the discretization of the lifting line

The wing is modeled using a lifting line method, where the wing is represented by a line and all the aerodynamic forces are computed at that line's location. However, usual applications of such a method imply the lifting line being fixed, which is not the case here. Since the discretization of the lifting line will likely change during the simulations (it is re-computed at each time step), proof needs to be given that changes in the discretization of a lifting line does not alter the numerical solution yielded by the method. In this section, proof will be given that a time-varying discretization of a lifting line has no impact on the numerical solution. The proof is given in this section for a continuous mapping but generalization to a discrete line is straightforward.

Proposition The displacement of the control points of a lifting line has no impact on the wake produced by such method, hence no impact on the aerodynamic forces.

The wake is characterized by the intensity of the circulation sheet $\boldsymbol{\gamma}(y, x)$, which is linked to the variations of the circulation $\Gamma(y, t)$ of the wing (in a straight, fixed wing) as :

$$\boldsymbol{\gamma}(y, x) = \begin{pmatrix} -\frac{\partial \Gamma}{\partial y} \\ -\frac{1}{U}\frac{\partial \Gamma}{\partial t} \\ 0 \end{pmatrix} = \begin{pmatrix} \gamma_x \\ \gamma_y \\ 0 \end{pmatrix}$$

We consider a lifting line as shown in figure 17 with known circulation $\Gamma(t, y)$. This line is parallel to the y axis and has a velocity U parallel to the x axis. The position y along the line is mapped to another variable η through a time-varying function :

$$y\,(t, \eta) : t \in \Re, \eta \in [0, 1] \rightarrow y \in \left[-\frac{b}{2}, \frac{b}{2}\right]$$

where b is the span of the wing. The wake will be independent of the (time-varying) mapping between the position y and the variable η if and only if :

$$\boldsymbol{\gamma}\,(t, \eta) = \boldsymbol{\gamma}\,(t, y\,(t, \eta))$$

for any function $y\,(t, \eta)$ and by computing $\boldsymbol{\gamma}$ only using variations of Γ with η.

Proof If the mapping is applied, the intensity of the circulation sheet has to be computed from fixed value of the η parameter. The following derivatives will be used :

$$\left.\frac{\partial \Gamma}{\partial t}\right|_{\eta} = \left.\frac{\partial \Gamma}{\partial y}\right|_{t} \left.\frac{\partial y}{\partial t}\right|_{\eta} + \left.\frac{\partial \Gamma}{\partial t}\right|_{y}$$

and

$$\left.\frac{\partial \Gamma}{\partial \eta}\right|_{t} = \left.\frac{\partial \Gamma}{\partial y}\right|_{t} \left.\frac{\partial y}{\partial \eta}\right|_{t}$$

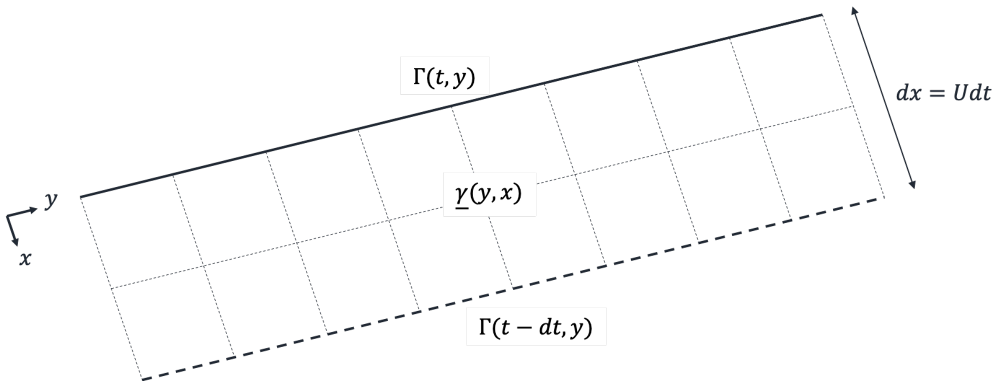

Figure 17: Representation of the lifting line used for the proof. The lifting line is the solid line and the thick dashed line represents its position one time-step dt before. The area between is the wake that is shed during this time-step.

The time variations of Γ for a fixed value of η will contribute to the sheet like shown in figure 18. That is, the Y component of the sheet's intensity can be reduced to a linear circulation $d\Gamma_y$ equal to :

$$d\Gamma_y = -\left.\frac{\partial\Gamma}{\partial t}\right|_\eta dt$$

Since γ_y and $d\Gamma_y$ are related like :

$$\gamma_y dS = d\Gamma_y dy$$

then, considering that $dS = dydx$ and $dx = Udt$, one founds :

$$\gamma_y = -\frac{1}{U}\left.\frac{\partial\Gamma}{\partial t}\right|_\eta = -\frac{1}{U}\left(\left.\frac{\partial\Gamma}{\partial y}\right|_t \left.\frac{\partial y}{\partial t}\right|_\eta + \left.\frac{\partial\Gamma}{\partial t}\right|_y\right)$$

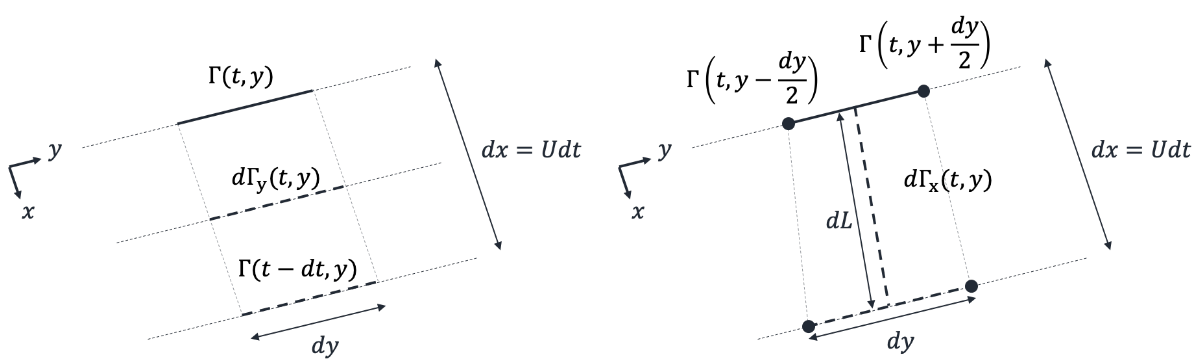

Figure 18: Representation of the two components of the circulation sheet : the component related to the time-variations of the circulation to the left and the one linked to the span-wise variations to the right

The component γ_x of the circulation sheet is related to the span-wise variations of the line's circulation. Taking the mapping into account, it can be reduced to a linear circulation $d\Gamma_x$ like :

$$d\Gamma_x = -\left.\frac{\partial\Gamma}{\partial y}\right|_t \left.\frac{\partial y}{\partial\eta}\right|_t d\eta$$

and, like before, it can be linked to the sheet's intensity with :

$$\gamma_x dS = d\Gamma_x dL$$

where dL is the distance the current point of the mapping has traveled during a time dt and dS is the surface of the parallelogram with base $dy = \frac{\partial y}{\partial \eta} d\eta$ and height $dx = U dt$, i.e. $dS = dy dx = U \frac{\partial y}{\partial \eta} dt d\eta$.

This distance can be computed with the velocity vector for a given η that will have two components. The first one is the velocity of the line in the x direction, that is $v_x = -U$. The second one is the velocity of the current point along the line and is caused by the changes in the mapping. This velocity will be along the y direction and will be given by $v_y = \left.\frac{\partial y}{\partial t}\right|_\eta$.

Therefore, in a time dt, the point will have traveled a distance equal to :

$$dL = \sqrt{v_x^2 + v_y^2}\, dt = \sqrt{U^2 + \left(\left.\frac{\partial y}{\partial t}\right|_\eta \right)^2}\, dt$$

and the contribution to the intensity of the sheet will be :

$$\gamma_x = -\frac{1}{U} \left.\frac{\partial \Gamma}{\partial y}\right|_t \sqrt{U^2 + \left(\left.\frac{\partial y}{\partial t}\right|_\eta \right)^2}$$

However, this contribution is not parallel to the x axis but parallel to the dL vector. So it has to multiply a unit vector $\hat{\mathbf{e}}_{dL}$ along dL :

$$\hat{\mathbf{e}}_{dL} = \frac{1}{dL} \begin{pmatrix} U \\ -\left.\frac{\partial y}{\partial t}\right|_\eta \\ 0 \end{pmatrix} = \frac{1}{\sqrt{1 + \left(\frac{1}{U}\frac{dy}{dt}\right)^2}} \begin{pmatrix} 1 \\ -\frac{1}{U}\left.\frac{\partial y}{\partial t}\right|_\eta \\ 0 \end{pmatrix}$$

The vectorial form of γ_x will then be :

$$\boldsymbol{\gamma}_x = \gamma_x \hat{\mathbf{e}}_{dL} = \left.\frac{\partial \Gamma}{\partial y}\right|_t \begin{pmatrix} -1 \\ \frac{1}{U}\left.\frac{\partial y}{\partial t}\right|_\eta \\ 0 \end{pmatrix}$$

and the sum of the two contributions $\boldsymbol{\gamma}_y$ and $\boldsymbol{\gamma}_x$, considering that the direction of $\boldsymbol{\gamma}_y$ is purely along the y axis, will then be :

$$\boldsymbol{\gamma} = \boldsymbol{\gamma}_y + \boldsymbol{\gamma}_x = -\frac{1}{U} \left(\left.\frac{\partial \Gamma}{\partial y}\right|_t \left.\frac{\partial y}{\partial t}\right|_\eta + \left.\frac{\partial \Gamma}{\partial t}\right|_y \right) \begin{pmatrix} 0 \\ 1 \\ 0 \end{pmatrix} + \left.\frac{\partial \Gamma}{\partial y}\right|_t \begin{pmatrix} -1 \\ \frac{1}{U}\left.\frac{\partial y}{\partial t}\right|_\eta \\ 0 \end{pmatrix} = \begin{pmatrix} -\frac{\partial \Gamma}{\partial y} \\ -\frac{1}{U}\frac{\partial \Gamma}{\partial t} \\ 0 \end{pmatrix}$$

which is the intensity that we expected to find. □

C Iterative process for the improvement of the lifting line

At each iteration, position and characteristics of each point of the quarter-chord line are updated. Starting from the current position of a point and the one of its two neighbors (part 1 of figure 19), the chord vector is re-projected so that it is orthogonal to the line passing through the two closest quart-chord line points (part 2 of figure 19). The points of the leading and trailing edges that are the closest to this line are then computed (part 3 of figure 19). Note that, since this is performed in 3D, the re-projected chord does not necessarily cross the leading and trailing edges, hence the closest point is found instead of the intersection. From the new chord and its corresponding points on the leading and trailing edges, the lifting line point is updated so that it properly stands at the quarter of the chord (part 4 of figure 19).

The quarter-chord line and the corresponding points in the leading and trailing edges being found, the computation of the chord and its orientation is straightforward for each point of the lifting line. For each point, the "line" vector is computed as the one linking the two adjacent points and the "up" vector is the cross product of the "chord" and "line" vectors. The velocity and angular velocity of each point of the lifting line is computed with first order finite differences with the current position and the one of the previous time step.

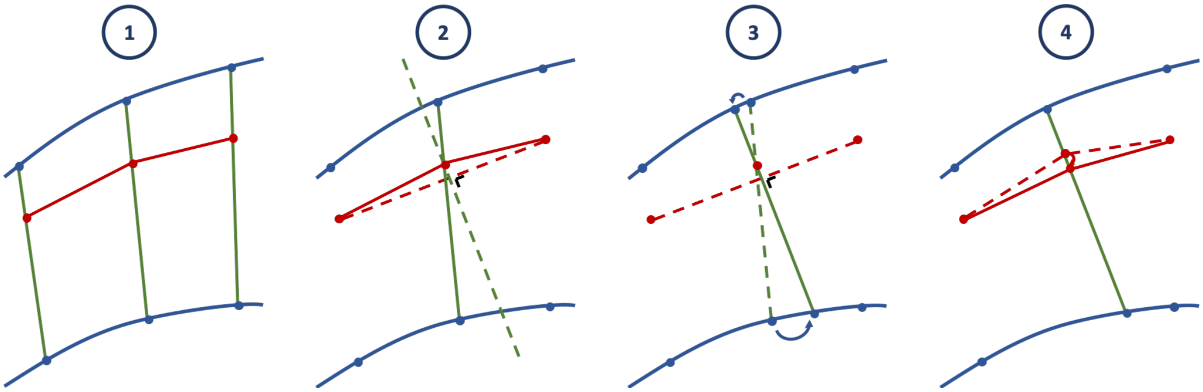

Figure 19: Steps followed for the improvement of each point of the lifting line

D Formula used for the control-volume computation of the forces

In [47], Noca presents a few equivalent formulations for the evaluation of aerodynamic forces on a body an incompressible flow. In this work, we use a formulation derived from the "impulse equation" from [47]:

$$\mathbf{F} = -\frac{1}{N-1}\frac{\mathrm{d}}{\mathrm{d}t}\int_V \mathbf{x}\times\boldsymbol{\omega}\,\mathrm{d}V + \int_V \mathbf{u}\times\boldsymbol{\omega}\,\mathrm{d}V + \oint_S \hat{\mathbf{n}}\cdot\boldsymbol{\gamma}_{imp}\,\mathrm{d}S \tag{17}$$

where $N = 3$ is the number of dimensions in the current application and

$$\boldsymbol{\gamma}_{imp} = -\frac{1}{N-1}\,\mathbf{u}\,(\mathbf{x}\times\boldsymbol{\omega}) + \frac{1}{N-1}\,\boldsymbol{\omega}\,(\mathbf{x}\times\mathbf{u})$$

Note that, when adapting the "impulse equation" from [47], we could omit certain terms considering that the control volume was not moving, and that the the integrals over the body surface were zero (since we use a lifting line and, as a singular line, it has no surface). We also omitted the terms related to the integral of viscous terms on the boundaries of the control volume, which produce negligible contributions.